CLM-P673

UKAEA

Preprint

THE PRECISION OF ELECTRON CYCLOTRON EMISSION MEASUREMENTS FROM DITE TOKAMAK

W. H. M. CLARK

CULHAM LABORATORY
Abingdon Oxfordshire

1983

CLM-P 673

THE PRECISION OF ELECTRON CYCLOTRON EMISSION MEASUREMENTS FROM DITE TOKAMAK

W.H.M. Clark

Culham Laboratory, Abingdon, Oxon., OX14 3DB, UK
(Euratom/UKAEA Fusion Association)

ABSTRACT

Corrections for the systematic errors associated with the measurements of electron cyclotron emission from DITE tokamak using a Michelson interferometer are considered under the following headings. (a) Finite optical depth: an isotropic reflection model is developed leading to a line-integral expression for the emission intensity which depends on the optical depth and the wall reflection coefficient. (b) Finite density and refraction: the error due to the distortion of the instrument antenna pattern is calculated from results of ray-tracing computations. (c) Relativistic resonance layer width: an expression is derived for the corresponding spatial error for emission perpendicular to the magnetic field. (d) Magnetic field corrections: an expression for the spatial error due to the poloidal and diamagnetic field contributions is given and its effect on the observed Shafranov shift is investigated. (e) Frequency response: the general principles of quasi-optics are applied to the Michelson interferometer demonstrating that a small-aperture blackbody oven may be used to calibrate the system. (f) Spatial resolution of the viewing optics: the equivalence of lens optics and waveguide antenna is shown both theoretically and experimentally and expressions are given for the resolution perpendicular to the viewing axis. (g) Frequency resolution: it is shown that the resolution of a Michelson interferometer can be better than that suggested by application of the Rayleigh criterion. These corrections are applied to experimental emission spectra and the derived electron temperature profiles compared with laser scattering measurements in a discharge where the plasma equilibrium is changing. The Shafranov shift of the corresponding temperature surfaces is shown to be in good agreement with that expected for the magnetic flux surfaces. Using the wall reflection model, the electron density profile is derived from the emission profile of the third harmonic cyclotron frequency.

(Submitted for publication in Plasma Physics)

May 1983

1. INTRODUCTION

The use of electron cyclotron emission, ECE, as a diagnostic for measuring the electron temperature profile across the major radius, T(R), in tokamak discharges is well established (COSTLEY et al., 1974; COSTLEY and TFR GROUP, 1977; BROSSIER et al., 1977; HUTCHINSON and KOMM, 1977; HOSEA et al., 1977; BAGDASAROV et al., 1979; TAIT et al., 1981). The principle whereby the radial variation of the toroidal magnetic field, B(R), and the blackbody nature of the emission enables the electron temperature to be spatially resolved was first given in detail by ENGELMANN and CURATOLO (1973) hereinafter referred to as EC. Provided certain assumptions hold, this elegant result enables the emission at the second harmonic of the electron cyclotron frequency to be interpreted in terms of T(R) where, as a fraction of the minor radius r, the spatial resolution is of order r/R.

The use to which such profile data is put by the tokamak physicist is dependent on an understanding of the errors inherent in the measurements. Random errors due to signal noise are often very small causing systematic errors to dominate the overall precision of the measurement.

In this paper these systematic errors are considered in detail and estimates obtained of the overall precision of T(R) measurements made on the DITE tokamak (PAUL et al., 1977). Although there are several methods for measuring ECE (BOYD, 1980), the work reported here solely concerns the Michelson interferometer technique (COSTLEY and CHAMBERLAIN, 1974). It is shown that by careful consideration of the relevant errors, minor radius profile data to an accuracy of order $(r/R)^2$ can be obtained, leading to a measurement of the configuration of the magnetic flux surfaces. Also, by considering emission at the

third harmonic in conjunction with a suitable wall reflection model, a measurement of the minor radius electron density profile can be derived.

In section 2 systematic errors relating to the physics of ECE are considered and estimates of their magnitudes derived. In section 3 the general principles of using quasi-optical techniques to measure ECE are reviewed leading to a description of experiments to calibrate the frequency response of a Michelson interferometer. In section 4 the error estimates and corrections are applied to experimental data illustrating the improved precision and extra profile information while in section 5 the implications of these corrections for ECE measurements on future tokamak experiments are considered.

2. SYSTEMATIC ERRORS ARISING FROM THE PHYSICS

2.1 Basic Theory

For ECE at the cyclotron frequency and its harmonics, i.e.

$$\omega = n\omega_c = n\frac{eB}{m} \qquad n = 1, 2, 3 \ldots \qquad \ldots (1)$$

the emitted intensity, $I(\omega)$ of a given mode of polarisation is at the blackbody level, viz:

$$I(\omega) = \frac{\omega^2 \kappa T}{8\pi^3 c^2} \qquad \ldots (2)$$

provided the electrons have a Maxwellian velocity distribution at temperature T and the optical depth, τ is large (BEKEFI, 1966a), i.e.:

$$\tau >> 1 \qquad \ldots (3)$$

In a tokamak the vacuum toroidal field, to within a few percent, is given by:

$$B(R) = \frac{B_o R_o}{R} \qquad \ldots (4)$$

where B_o is the value of B on the axis $R = R_o$.

When observed perpendicular to B in the meridian plane, the emission at a given frequency is narrowly confined to the resonance layer at a given radius (EC), such that if the optical thickness criterion (3) holds then relations (2) and (4) provide a one-to-one transformation between $I(\omega)$ and $T(R)$.

For thermal tokamak discharges this simple model applies, within certain limits, to emission of the second harmonic extraordinary (E) mode and hence measurements of the emission at this harmonic are used as a diagnostic of $T(R)$. However often these assumptions are not rigorously valid and consequently the precision of the $T(R)$ data is called into question. In the following sub-sections each assumption is examined in more detail than previously (CLARK, 1980) and the consequences of its violation discussed. The resulting systematic errors are classified under (a) temperature corrections and (b) spatial corrections.

2.2 Finite Optical Depth

If (3) is invalid then the resonant layer is optically thin and radiation reflected off the vacuum chamber walls must be taken into account. Previous methods (COSTLEY et al., 1974; HUTCHINSON and KOMM, 1977) have used the ideal model of plane parallel walls. A more realistic assumption is that wall reflections scramble the radiation sufficiently to produce a background, isotropic intensity $I_o(\omega)$.

Thus for any point with co-ordinate z on the cylindrical resonance surface R, (see Fig 1) the intensity of emission in direction (θ,ϕ) to B for each polarisation mode is a solution of the ray transport equation (BEKEFI, 1966a)

$$I(R,z,\theta,\phi) = I_b(R,z)\left[1 - e^{-\tau}\right] + I_o(R)\, e^{-\tau} \qquad \ldots (5)$$

where τ is a function of the form: $\tau_n(R,z,\theta)/\sin\theta\cos\phi$ for each polarisation,* the relation $\omega(R)$ is given by (1) and (4) and I_b is the local blackbody emission (2). The background intensity I_o may be determined by a power balance between radiation emitted from the surface and radiation absorbed both by the surface and the walls (ROSENBLUTH, 1970; EC):

$$\iint I_b(1 - e^{-\tau})\sin\theta\cos\phi\, d\Omega\, dS =$$

$$I_o\left[\pi A(1 - \rho) + \iint (1 - e^{-\tau})\sin\theta\cos\phi\, d\Omega\, dS\right] \qquad \ldots (6)$$

---

*For clarity the polarisation mode subscript is omitted from equations (5) to (9).

where the integrations are over the surface area of emission and a solid angle of 2π. The parameter ρ is an average wall reflection coefficient which takes into account conversion between polarisation modes on reflection and A is the area of the vacuum chamber wall.* A general treatment of the problem involves a set of simultaneous equations of (5) and (6) for both polarisation modes and the reflection coefficient becomes a 2 x 2 matrix [TAMOR, 1981]. However for the second and third harmonics, emission of the ordinary (O) mode is very weak for experimental conditions in DITE such that for the E mode emission, equation (6) is a good approximation for I_o.

Solid angle integration of (6) leads to:

$$I_o = \frac{\int I_b \, \langle 1-e^{-\tau} \rangle \, dz}{(1 - \rho) \frac{A}{4\pi R} + \int \langle 1-e^{-\tau} \rangle \, dz} \qquad \ldots (7)$$

where $\langle \; \rangle$ denotes the solid angle average value. When $\tau << 1$ this value reduces to $\bar{\tau}_n$ as defined by EC (see below). If this result is compared with the corresponding expression for plane parallel reflectors viz:

$$I_o = \frac{I_b(1 - e^{-\tau})}{(1 - \rho e^{-\tau})}$$

---

*ρ and A implicitly contain the effect of radiation lost through holes in the wall. To include these explicitly the factor $(1-\rho)A$ should be replaced by $(1-\rho)A_W + A_H$ where ρ is now the reflectivity of the wall material and A_W and A_H the total areas of the holes and the wall respectively.

it can be seen that, in the limit of small τ, the factor $(1 - \rho)$ is effectively multiplied by the ratio of the wall area to the resonance surface area and the optical depths become appropriately averaged values.

For metal walls and millimetre wavelength radiation $(1 - \rho) \ll 1$, hence consideration of (5) and (7) indicates that the level of emission in the plane $z = 0$, falls into 3 regimes.

a) Optically thick

If $\tau \gg 1$ then expression (5) reduces to: $I(\omega) = I_b(R,0)$

b) Optically thick by means of reflections

If $$1 \gg \tau \text{ and } \int \bar{\tau}_n \, dz \gg (1 - \rho) \frac{A}{4\pi R}$$

then equation (7) reduces to:

$$I(\omega) = \frac{\int I_b \, \bar{\tau}_n \, dz}{\int \bar{\tau}_n \, dz} \qquad \ldots (8)$$

c) Optically thin with reflections

If $$(1 - \rho) \frac{A}{4\pi R} \gg \int \bar{\tau}_n \, dz$$

then equation (7) reduces to:

$$I(\omega) = \frac{4\pi R}{(1 - \rho)A} \int I_b \, \bar{\tau}_n \, dz \qquad \ldots (9)$$

To estimate the emission for the E mode second and third harmonics, EC give the following approximation for $\langle 1-e^{-\tau} \rangle$ and hence $\bar{\tau}_n$:

$$\left.\begin{aligned} \langle 1-e^{-\tau} \rangle_n &= \frac{\bar{\tau}_{nE}}{1 + \bar{\tau}_{nE}} \\ \bar{\tau}_{nE} &= \tau_{nE}/F_{nE} \end{aligned}\right\} \qquad \ldots (10)$$

where:

$$\left.\begin{aligned} \tau_{2E} &= 4\pi^2 \frac{R}{\lambda} \frac{\omega_p^2}{\omega^2} \frac{\kappa T}{m c^2} \\ F_{2E} &= \frac{5}{8} \end{aligned}\right\} \qquad \ldots (11)$$

and

$$\left.\begin{aligned} \tau_{3E} &= \frac{243}{32} \frac{\kappa T}{m c^2} \tau_{2E} \\ F_{3E} &= \frac{105}{128} \end{aligned}\right\} \qquad \ldots (12)$$

Here ω_p is the electron plasma frequency and λ the vacuum wavelength of the emission.

In DITE, for the second harmonic E mode and reasonable values of T and ω_p, regime (a) is valid in the centre of the discharge and regime (b) near the edge. Thus substitution of (10) and (11) into (8) indicates that the radiation temperature near the edge is a weighted average across the resonance surface, i.e.,

$$\overline{T(R)} = \frac{\int_{-b}^{+b} n_e(R,z)\ T^2\ (R,z)\ dz}{\int_{-b}^{+b} n_e(R,z)\ T(R,z)\ dz} \qquad \ldots (13)$$

where n_e is the electron density.

However for the third harmonic E mode emission in DITE discharges, regime (c) is valid. Thus substitution of (10) and (12) into (9) leads to:

$$\frac{I_o(R)}{R} = K \int_{-b}^{+b} n_e(R,z)\ T^3(R,z)\ dz \qquad \ldots (14)$$

where
$$K = \frac{648}{35} \frac{R_o}{\lambda_o} \frac{1}{(1-\rho)A} \frac{e^2}{\varepsilon_o} \left(\frac{\kappa}{m\ c^2} \right)^3$$

In the constant K the symbols have their usual M.K.S. values and λ_o is the wavelength of the radiation emitted at $R = R_o$. Thus if T(r) is known, $n_e(r)$ can be derived from an Abel inversion (BRACEWELL, 1965) of the LHS of equation (14) since, if cylindrical symmetry is assumed,

$$r^2 = z^2 + (R - R_o)^2 \qquad \ldots (15)$$

Application of these expressions to experimental data is given in section 4.4.

2.3 Finite Density Corrections and Refraction

The linear dependence of τ on n_e, (11) and (12), is only correct at low density, i.e. $\omega_p^2 << \omega^2$, for which the refractive index, N of the radiation is unity. For finite density, the value of N_E for the E mode propagating perpendicular to B is given by STIX (1962):

$$N_E^2 = \frac{(1 - \omega_p^2/\omega^2)^2 - \omega_c^2/\omega^2}{1 - \omega_p^2/\omega^2 - \omega_c^2/\omega^2} \qquad \ldots (16)$$

Thus for the second harmonic, the low density (i.e. $N_E = 0$), cut-off occurs for

$$\omega_p^2 = 2\omega_c^2 \qquad \ldots (17)$$

As the density approaches cut-off τ is slightly modified from the low density scaling until just below cut-off, at which it drops to zero (BORNATICI et al., 1981). However below cut-off, refraction of ECE ray paths (fig 2) can cause radiation emitted from the cooler regions of the plasma to be detected by viewing optics designed to view in the z = 0 plane.

In order to quantify this effect, ray-tracing computations have been carried out (NAVE and CLARK, 1980) of the extreme rays detected by the optics using density profiles of the form:

$$n_e(r) = n_o(1 - (r/a)^p)^q \qquad \ldots (18)$$

and the magnetic field variation (4) to determine N_E for the second harmonic from (16). From these computations, the dimension D of the antenna pattern in the plane perpendicular to B is calculated as a function of the position of the resonance layer for the DITE antenna geometry (see section 3.3). The results for different profile shapes and densities are plotted in figs 3(a) and 3(b) where n_o is expressed as a fraction of the cut-off density n_c at r = 0, as calculated from (17).

These curves indicate that for peaked profiles ($p \sim 2$, $q \sim 4$), significant refraction occurs as the central density approaches 80% of cut-off, in that D is double the vacuum value on the far side of the plasma. For flat profiles ($p \sim 2$, $q \sim 0.5$) the effect is weaker except that the region of cut-off emission is larger as the density exceeds cut-off in the centre. For optically thick regions of the plasma, the corresponding "antenna temperature" may be estimated by calculating the surface average value of T(R,z) over the region defined by D (allowing for any region where the emission is cut-off). However since the emission is no longer localised for optically thin regions, refraction does not significantly affect the evaluation of $\overline{T(R)}$ given by (13), except when the emission is cut-off in the centre (see section 4.2).

B. SPATIAL CORRECTIONS

2.4 Relativistic Resonance Layer Width

For emission close to perpendicular to B, i.e. $\cos\theta < \sqrt{\kappa T/mc^2}$, the physical thickness of the resonance layer due to the relativistic electron mass is $\sim R\kappa T/mc^2$. For high temperatures in this situation, the radiation at a given frequency is emitted from a broad layer as illustrated in fig 4(a) where the absorption coefficient, α, is plotted as a function of R. The variation of T within this layer depends, to first order, on the magnitude of the normalised temperature gradient, ∇_T where:

$$\nabla_T = \frac{R}{T}\frac{dT}{dR} \qquad \ldots (19)$$

This variation gives rise to an error in T(R) which can be interpreted in terms of an error, δR, in the $\omega(R)$ transformation (1) and (4). δR can be estimated by considering the correct solution of the ray transport equation for emission at ω_1, (neglecting reflected radiation) viz: (BEKEFI, 1966a)

$$I(\omega_1) = \int_0^{\tau_0} I_b\, e^{-\tau}\, d\tau \qquad \ldots (20)$$

where the variable τ is obtained by integrating α backwards along the ray path,

$$\tau(R) = -\int_{R_1}^{R} \alpha\, ds \qquad \ldots (21)$$

see fig 4(a). In the low density limit, the integral (21) for the second harmonic E mode can be expressed as (BORNATICI, 1980):

$$\tau = \tau_o \frac{8}{15\sqrt{\pi}} \int_o^y e^{-x} x^{5/2} dx \qquad \ldots (22)$$

where τ_o is given by (11) and y is the normalised width parameter of the resonance layer:

$$y = \frac{m c^2}{\kappa T} \left(\frac{R_1 - R}{R_1} \right) \qquad \ldots (23)$$

To first order, the variation of I_b within the resonance layer is:

$$I_b(y) = I_b(R_1) \left[1 - y \frac{\kappa T}{m c^2} \nabla_T \right] \qquad \ldots (24)$$

Thus substitution of (24) and the inverse of (22) into (20) leads to:

$$I(\omega_1) = I_b(R_1) \left[1 - e^{-\tau_o} - \nabla_T \frac{\kappa T}{m c^2} F(\tau_o) \right] \qquad \ldots (25)$$

where $$F(\tau_o) = \int_o^{\tau_o} y(\tau) e^{-\tau} d\tau \qquad \ldots (26)$$

In fig 4(b) the result of a numerical integration for $F(\tau_o)$ is shown and in the appendix a useful analytic approximation of F is derived for $\tau_o >> 1$.

For the evaluation of δR, the self-absorption term can be dropped as this relates to the finite optical depth correction of section 2.3. Thus using (4) and the incremental approximation to (19) gives:

$$\frac{\delta R}{R} = - \frac{\kappa T}{m c^2} F(\tau_o) \qquad \ldots (27)$$

For $\tau_o >> 1$, $F(\tau_o)$ gradually decreases such that for high temperatures and moderate densities δR is considerably smaller than the physical width of the layer as determined by the integrand of (22). It has been pointed out (BARTLETT and COSTLEY, 1979) that this advantageous effect is due to emission from the bulk of the layer behind R_1, being absorbed because of the large value of α.*

2.5 Magnetic Field Corrections

For the tokamak configuration, corrections to the vacuum magnetic field (4) due to plasma current and diamagnetism are of order $(r/R)^2$ (CONNOR and HASTIE, 1976). For $r/R << 1$, these may be calculated from an analytic solution of the MHD equilibrium to second order in r/R. The magnitude δB of the total field correction is then given by

$$\frac{\delta B}{B_o} = \frac{\tilde{B}}{B_o} + \frac{1}{2} b_\theta^2 \qquad \ldots (28)$$

where the normalised poloidal field $b_\theta(r)$ is derived from the plasma

---

*This favourable situation does not apply for oblique emission, i.e. $\cos\theta > \sqrt{\kappa T/mc^2}$, as the layer thickness is determined by the doppler shift. Then the profile of α is broader and symmetrical about R_1 leading, if $\tau_o >> 1$, to a larger correction of the opposite sign, (i.e. $\Delta R \sim R \cos\theta$).

current density $j(r)$:

$$b_\theta(r) = \frac{\mu_o}{B_o} \int j\, r\, dr \qquad \ldots (29)$$

and the diamagnetic contribution, $\tilde{B}(r)$ is given by:

$$-\frac{1}{B_o}\frac{d\tilde{B}}{dr} = \frac{1}{2}\left\{\frac{d\beta_\perp}{dr} + \frac{db_\theta^2}{dr}\right\} + \frac{b_\theta^2}{r} \qquad \ldots (30)$$

where the plasma perpendicular pressure $p_\perp(r)$ is normalised to:

$$\beta_\perp = \frac{2\mu_o\, p_\perp}{B_o^2} \qquad \ldots (31)$$

Although the absolute magnitude of these corrections is small their relative variation across the plasma profile is of order r/R and is important when considering how the electron isothermal surfaces are affected by the shift (SHAFRANOV, 1962) of the centres, $\Delta(r)$, of circular magnetic flux surfaces of radius r, where:

$$-\frac{d\Delta}{dr} = \frac{r}{2R_o}\left\{\frac{\bar{\beta}_\parallel + \bar{\beta}_\perp - (\beta_\parallel + \beta_\perp) + \overline{b_\theta^2}}{b_\theta^2}\right\} \qquad \ldots (32)$$

and surface average quantities are defined as

$$\bar{\beta} = \frac{\int \beta\, r\, dr}{\int r\, dr}$$

If we assume that the isothermal surfaces can be identified with the flux surfaces as shown in fig 5(a), then the shift of their centres (32) can be determined from the measured T(R) profile provided correction (28) is applied consistently (see fig 5(b)).

Thus the shift Δ_{ece} observed from the ECE profile assuming a vacuum magnetic field, is related to the true shift Δ by

$$\Delta_{ece} = \Delta - R_o \frac{\delta B}{B_o} \qquad \ldots (33)$$

In order to see how this discrepancy between Δ_{ece} and Δ varies with plasma parameters, (30) may be substituted into the differential of (28):

$$\frac{d\Delta_{ece}}{dr} = \frac{d\Delta}{dr} + R_o \left\{ \frac{b_\theta^2}{r} + \frac{1}{2} \frac{d\beta_\perp}{dr} \right\} \qquad \ldots (34)$$

Thus the relative importance of the correction terms on the RHS of (34) depends on the magnitudes of the poloidal beta, β_p and the edge safety factor, q_a where

$$\beta_p = \frac{1}{2} \frac{(\bar{\beta}_\parallel + \bar{\beta}_\perp)}{b_\theta^2(a)} \qquad \ldots (35)$$

and

$$q_a = \frac{a}{R_o \, b_\theta(a)} \qquad \ldots (36)$$

This is conveniently demonstrated by considering the ideal model for the plasma column of a uniform current density and a parabolic,

isotropic pressure profile (i.e. radial variation (18) with p = 2 and q = 1). Then the solution to (32) is

$$\Delta = \frac{r^2}{8R_o}(4\beta_p + 1) \qquad \ldots (37)$$

and integrating (34):

$$[\Delta(r) - \Delta(a)]_{ece} = [\Delta(r) - \Delta(a)] \left\{1 - \frac{4(1 - 2\beta_p)}{q_a^2(1 + 4\beta_p)}\right\} \ldots (38)$$

Figure 6 illustrates how the ECE shift is enhanced or diminished according to whether the plasma is diamagnetic ($\beta_p > 1$) or paramagnetic ($\beta_p < 1$). For this model $\delta B(r)$ is constant for $\beta_p = 1/2$, whereas in general for $\beta_p \sim 1$ the plasma diamagnetism is very small and the only correction is that of b_θ^2 which diminishes as q_a increases. In section 4 these corrections are applied to experimental data.

3. SYSTEMATIC ERRORS ARISING FROM THE MEASUREMENT TECHNIQUE

3.1 General Principles of Quasi-Optical Techniques

Compared with microwave heterodyne techniques (see eg EFTHIMION, 1979), using a Michelson interferometer to measure ECE has the advantage of working over a wide frequency range. However for low field tokamaks ($B_o < 3T$), the aperture-to-wavelength ratio, d/λ is typically no larger than 30 and consequently the performance of the

instrument cannot be adequately described in terms of geometrical optics (MARTIN and LESURF, 1978). A simple model applicable at these wavelengths is that of the oversize waveguide where the propagation of radiation within the instrument is analysed in terms of its eigenmodes (COSTLEY et al., 1980). If $N(\omega)$ modes of a given polarisation can propagate in the waveguide and the antenna pattern for each mode is filled with blackbody radiation, the total power dP transported is determined by equipartition theory (BEKEFI, 1966b).

$$dP = N(\omega) \frac{\kappa T}{2\pi} d\omega \qquad \ldots (39)$$

For the simple case of a square cross-section waveguide of aperture d, each mode (m,n) is represented by lattice points ($\pm m\pi/d$, $\pm n\pi/d$) in perpendicular wave-number space (k_x,k_y). Those points lying outside the waveguide cut-off circle:

$$\left(\frac{\omega}{c}\right)^2 = \left(\frac{\pi}{d}\right)^2 (m^2 + n^2) \qquad \ldots (40)$$

represent evanescent modes (fig 7(a)). If ω_c is the cut-off frequency for the fundamental (1,0) mode, then as ω/ω_c increases, $N(\omega)$ increases in discrete steps (fig 7(b)) such that for large values the mode spectrum tends to a continuum and

$$N(\omega) = \frac{1}{2} \pi \left(\frac{\omega}{c}\right)^2 \left(\frac{d}{\pi}\right)^2 \qquad \ldots (41)$$

Substituting (41) into (39) gives the same result as that calculated from (2) across an area of d^2 and a solid angle of 2π. Thus a convenient definition of the frequency response $F(\omega)$ of this "quasi-optical" system for a given polarisation is:

$$F(\omega) = \frac{4N(\omega)}{\pi} \Big/ \left(\frac{\omega}{\omega_c}\right)^2 \qquad \ldots (42)$$

which is clearly not "flat" for low values of ω/ω_c.

A further consideration when applying this model to a practical instrument is that radiation from oblique angles is not transmitted by the viewing optics (section 3.3). Thus although a large number of modes can propagate in the instrument at the frequency of interest, only those low order modes propagating within the acceptance angle γ of the viewing axis, transport blackbody radiation to the detector. Consequently the corresponding cut-off circle now becomes:

$$\left(\frac{\omega}{c} \sin \gamma\right)^2 = \left(\frac{\pi}{d}\right)^2 (m^2 + n^2) \qquad \ldots (43)$$

Applying (43) to $F(\omega)$, results in a reduction of the effective cut-off frequency to $\omega_c \sin\gamma$. For the work reported here, $d \sim 50$mm, $\omega/\omega_c \sim 40$ and $\gamma \sim 3°$. Thus the instrument is operating in the regime where only two or three modes contain blackbody radiation. This is a direct consequence of having to limit the instrument étendue to provide a reasonable spatial resolution in the perpendicular directions.

Although the above results are derived for a square waveguide, the principles apply to any "quasi-optical" system. For example if lenses

or spherical mirrors are considered, the corresponding eigenmodes are those of gaussian optics (MARTIN and LESURF, 1978).

3.2 Calibration of the Michelson Interferometer

Figure 8 shows the schematic arrangement of the apparatus used to measure ECE from DITE tokamak. The radiation is observed via a wedged shaped window of crystal quartz (wedge angle 3°, dia. 40mm) in the meridian plane of the tokamak. The viewing optics (see section 3.3) select the E mode polarisation for transmission to the interferometer via two plane reflecting bends, which preserve the polarisation direction, and a cylindrical brass light pipe of length 3m and dia. 50mm. The two-beam polarisation-type Michelson interferometer (MARTIN and PUPLETT, 1970) also selects the E mode polarisation and scans sinuosoidally through a path difference of 32mm at a frequency of 35Hz. An indium antimonide detector cooled to 4.2°K (QMC INSTRUMENTS) is used to detect the radiation and the processing of the data is carried out by a dedicated DEC LSI-11 minicomputer via an ADC and memory in a CAMAC dataway.

In order to measure $F(\omega)$ for such a system, a suitable blackbody source of radiation is required which couples to the viewing optics in the same way as the plasma ECE. Other workers in this field have used large area sources at liquid nitrogen temperature (77°K) (TAIT et al., 1981; HUTCHINSON and KISSEL, 1979; SAKAI et al., 1980) which require a large number of scans to achieve a reasonable signal-to-noise ratio. In this work a source at 1000°K, i.e. three times the background temperature, is used to overcome this problem. However it suffers from the disadvantage of having a small aperture (dia. 10mm) and thus requires careful matching to the viewing optics. Figure 9 shows the

arrangement of the source, (ADVANCED KINETICS oven BB1000) where the matching is achieved by a 1 in 8 copper conical taper and the quartz window is identical to the tokamak observation window.

The matching criterion is easily understood if the general principles of section 3.1 are used. Thus for a square source aperture of dimension d_s, all modes below cut-off contain blackbody radiation. For an ideal taper between dimension d_s and d, each mode retains this power flux as its angle of propagation with the axis diminishes (i.e. for $d > d_s$). Thus provided the radius of the cut-off circle for the aperture (40) is greater than that of the cut-off circle for the interferometer acceptance angle (43), viz.

$$\frac{d_s}{d} > \sin \gamma \qquad \ldots (44)$$

all of the modes which the instrument can accept are detected at a blackbody level. To allow for power scattered between high and low order modes within the wide end of an imperfect taper, criterion (44) needs to be satisfied by a large margin. In this work $d_s/d \sim 1/5$ and $\sin \gamma \sim 1/20$, which should be sufficient, even for cylindrical geometry. The geometric optics analogue of (44) is that the étendue of the source must be greater than the étendue of the instrument.

Figure 10 shows the resulting calibration curve, $F(\omega)$ obtained using the blackbody source and the lens viewing optics described in section 3.3. The experimental curve and error bars were obtained by averaging 7 spectra where each spectrum is the fourier transform of the average of 50 interferograms. Also shown is the theoretical response curve (42) derived for a cylindrical waveguide (MORENO, 1948) with a

fundamental cut-off frequency $\omega_c/2\pi$ = 75GHz and the resulting spectrum convolved with the appropriate instrument function (see section 3.4). For an aperture d = 40mm, ω_c corresponds to an acceptance angle γ = 3.3°. This is in good agreement with the acceptance angle defined by the lens optics, thus illustrating the usefulness of oversize waveguide principles for determining the performance of a quasi-optical system at these wavelengths.

3.3 Spatial Resolution of the Viewing Optics

Although the interferometer itself has a well collimated antenna pattern, of divergence ~ 3°, this may be degraded in the plasma by irregular reflections in the light pipe assembly allowing radiation collected from oblique angles (i.e. high order modes) to be scattered into low order modes and thus be detected. To prevent this it is necessary to define the antenna pattern and polarisation of the radiation at the observation window. In this work two methods have been used.

a) Lens-stop collimator

This device (fig 11(a)) is based on simple lens optics formulae where the spatial dimension, D of the antenna pattern is given by:

$$D = d + (L - 2f)\frac{e}{f} \qquad \text{for } L > 2f \qquad \ldots (45)$$

where e is the diameter of an aperture in the focal plane of two lenses with focal length f. Such a system is used routinely for measurements on DITE with f = 90mm, d = 40mm and e = 10mm, although geometric optics

is not applicable for $\lambda \sim 2$mm. However the properties of the system are found to be adequately described by (45) in that the detected power level is independent of e for e > 10mm (i.e. divergences > 3°). This also suggests that the mode scattering in the light pipe is small.

b) Fundamental waveguide antenna

This device is based on the principles of diffraction optics. A section of fundamental mode guide within a waveguide transmission system ensures that a horn antenna is operating in its fundamental mode over the frequency range of interest. Using a simple diffraction model for the antenna pattern (COSTLEY et al., 1980), we have (see fig 11(b)):

$$\left.\begin{array}{lll} \text{near field:} & D = d + L\dfrac{\lambda}{d} & \text{for } L < \dfrac{d^2}{\lambda} \\ \text{far field:} & D = 2L\dfrac{\lambda}{d} & \text{for } L > \dfrac{d^2}{\lambda} \end{array}\right\} \quad \ldots (46)$$

Substituting the radial variation $\lambda(R)$ implicit in (4) into (46) leads to an optimum value for the horn aperture d_o

$$d_o = \frac{L_o}{2}\sqrt{\frac{\lambda_o}{R_o}} \qquad \ldots (47)$$

where L_o is the major radius of the antenna and λ_o the wavelength at R_o. This corresponds to the plasma being positioned at the boundary between the near and far field regions of (46). In this situation D(L) has a parabolic variation with a maximum of $2d_o$ at $L_o/2$.

To test this idea, measurements were made using a horn of aperture

40mm which tapers down to a section of rectangular waveguide, 30mm in length operating in the fundamental mode over the range 90 to 180GHz for the E mode polarisation. After this there is a taper up to 10GHz band waveguide which transmits the signal over 2m to where it is coupled to the interferometer aperture by a taper and phase-correcting lens.

Figure 12(a) shows the relative intensities of broad-band, non-thermal ECE spectra taken from nominally identical discharges with both types of viewing optics where the lens optics spectrum has been divided by its calibration curve (fig 10). Over the bandwidth of the fundamental waveguide, the frequency response of the waveguide antenna can be determined by the ratio of the two spectra. The result is shown in fig 12(b) along with the theoretical response (40) for the fundamental section of waveguide. There is good agreement between the experimental and theoretical cut-off frequencies but the theory does not take into account the significant attenuation in the waveguide at frequencies close to cut-off, which is thought to be the main source of discrepancy between the two curves. The absolute intensity of the waveguide spectrum is at least a factor of 5 smaller than the lens optics spectrum (see the vertical scale of fig 12b). Consequently it is difficult to calibrate the waveguide antenna directly using the blackbody oven since the signal-to-background ratio is reduced from 3 to < 0.6.

3.4 Frequency Resolution Error of a Michelson Interferometer

The frequency resolution due to the finite maximum path difference, ℓ gives rise to a radial spatial resolution δR.

Application of the Rayleigh resolution criterion (CHANTRY and FLEMMING, 1976) gives $\delta R/a \sim 30\%$ for $\ell \sim 30$mm. However in the case of a smooth T(R) profile this is an over-estimate as can be seen by the following argument.

To lowest order

$$\frac{\delta R}{R} = - \frac{\delta I}{\omega} \Big/ \frac{dI}{d\omega} \qquad \ldots (48)$$

where δI is the difference between the true spectrum $I(\omega)$ and the measured spectrum $I_i(\omega)$. The measured spectrum is determined by the convolution integral:

$$I_i(\omega) = \frac{1}{2\pi} \int_{-\infty}^{+\infty} I(\omega - \omega')\, S(\omega')\, d\omega' \qquad \ldots (49)$$

where $S(\omega)$ is the instrument function which, if it has a bandwidth appreciably less than $I(\omega)$, allows a Taylor expansion of the integrand in (49), viz,

$$I_i(\omega) \sim I(\omega) + \frac{1}{2\pi} \frac{dI}{d\omega} \int \omega' S \, d\omega' + \frac{1}{4\pi} \frac{d^2 I}{d\omega^2} \int \omega'^2 \, S \, d\omega' \quad \ldots (50)$$

Following the usual practice in fourier transform spectroscopy, $I_i(\omega)$ is apodised by multiplying the interferogram, $I_i(t)$, with the window function: $\cos^2(\pi t/2t_o)$ where $t_o = \ell/c$. For an ideal fourier transform interferometer this leads to an instrument function,

$$S(\omega) = \frac{t_o \sin \omega t_o}{\omega t_o \left\{1 - \left(\frac{\omega t_o}{\pi}\right)^2\right\}} \qquad \ldots (51)$$

Substitution of (51) into (50) causes the second term to vanish such that to lowest order, $\delta R = 0$ in (48). To next order

$$\delta I = \frac{\pi^2}{4t_o^2} \frac{d^2 I}{d\omega^2} \qquad \ldots (52)$$

Since the higher order even integrals in (50) do not converge, $dI/d\omega$ and hence dT/dR must be sufficiently smooth for (52) to be valid. If this is the case the resolution error (52) can be estimated by multiplying the interferogram with the window function: $(\pi t/2t_o)^2 \cos^2(\pi t/2t_o)$ and fourier transforming the result.

Since it is a second order correction, (52) can be small over most of the profile (an example is given in section 4). However for a practical instrument, imperfections may lead to an asymmetrical instrument function such that the first order term in (49) no longer cancels giving rise to a systematic frequency shift and consequently δR is no longer zero.

4. EXPERIMENTAL DATA

4.1 Comparison with Laser Scattering

In order to calculate and check the corrections discussed in the previous sections it is necessary to have data on the density profile, $n_e(r)$ and an independent measure of $T(R)$. On DITE these data are provided by a laser scattering diagnostic (PRENTICE, 1978) which

provides single point measurements on each of a series of nominally identical discharges, and a 2mm microwave interferometer which provides line average measurements of the density during each discharge.

Comparison between the ECE and laser T(R) profiles can be problematical because (i) possible variation of discharge conditions, (ii) the two measurements are made on different timescales (i.e. 8ms and 25ns respectively) and (iii) an accurate calibration of the absolute ECE intensity measured by the Michelson interferometer is difficult. Thus the comparison involves a least-squares fitting of the ECE profile to the laser data using the absolute ECE intensity factor as a free parameter. Since photon statistics provide error bars for the laser data, a statistical measure of the agreement between the two profiles is provided by the normalised χ^2 parameter (LEWIS, 1963) assuming no other random errors are involved.

Figure 13 shows such a comparison between the two profiles measured in a set of discharges (a) before and (b) during a pulse of neutral beam heating. The least squares fitting for the intensity factor is applied to all of the laser data giving a χ^2 value of 1.2 for 21 points. The expected value of χ^2 is 1 with a standard deviation of 0.32 indicating a good measure of agreement. Each of the corrections discussed in the preceding sections have been applied to the ECE profiles but only the frequency calibration $F(\omega)$, produced a significant improvement in χ^2 (see next section). The result of not applying this is shown by the dashed profiles for which $\chi^2 = 2.4$.

4.2 Quantative Estimate of the Corrections

As in section 2 systematic corrections are classified under corrections δT to T and corrections δR to R. In

fig 14(a) quantative estimates of the four $\delta T/T$ corrections are shown for the profile in fig 13(b). The evaluation of the finite optical depth correction is discussed in section 4.4. The refraction correction was estimated by finding the line average temperature of the measured T(R) over the antenna dimension D derived from ray tracing data similar to fig 3 but using the relevant $n_e(r)$ profile (see section 4.4). This estimate is no longer valid outside the region $\tau > 1$ for which the optical depth correction is dominant. To show its relative variation across the profile, the frequency response correction has been normalised to unity at $R_o = 1.17$m. The frequency resolution error was derived from (52) and tends to be small except near the edges of the profile where d^2T/dR^2 gradients are large. The smoothness of T(R) is probably due to the relatively coarse time resolution of the instrument which tends to average any rapid fluctuations of T(R). Apart from the frequency response, the estimation of these corrections relies on them being small (< 15%) which is true over 2/3 of the profile.

Figure 14(b) illustrates the corresponding $\delta R/R$ corrections which in general are an order of magnitude smaller. For this particular profile, $\beta_p \sim 1$ (see section 4.3) and consequently the plasma magnetic field correction is very small. For the angular divergence of the lens optics, the relativistic resonance layer width correction (27) applies to the central region of the discharge and also tends to be small because $\kappa T/mc^2 << 1$. By comparison the vacuum ripple field correction to (4) which is due to the discrete nature of the toroidal field coils, is relatively large, rising to 3% on the outside edge. This was calculated along a major radius midway between adjacent DITE coils in the meridian plane using a numerical solution for the vacuum field (MARTIN, 1976).

In general, apart from the frequency response, these corrections in DITE are very small over most of the profile.

4.3 Measurements of the Temperature Surfaces

During the neutral beam heating pulse, the temperature profile exhibits a clear asymmetry when compared with its shape before neutral beam heating. To check if this distortion is consistent with the expected change in plasma equilibrium, the following analysis of the profiles was carried out. For each profile measured at the two times of interest over a series of discharges, all the appropriate corrections were applied, except the plasma magnetic field correction, (28), and the centres $\Delta_{ece}(r)$, of the temperature surfaces (assumed to be circular cross-section) were calculated according to the prescription in fig 5(a). Δ_{ece} was related to the position of the plasma current axis deduced from magnetic flux loop measurements, (in DITE this is controlled by a feedback circuit but there is an uncontrolled variation of up to 10mm from discharge to discharge during the neutral beam pulse). The absolute position of the ECE axis, i.e. Δ_{ece} at $r = 0$, is determined by the value of B_o which was calculated from the current measured in the toroidal field coils. The results are shown in fig 15 where the error bars represent the standard error of the average Δ_{ece} over 20 profiles.

In order to calculate the expected Δ_{ece} (33) it is necessary to calculate $\Delta(r)$ from profile data of $\beta_{\parallel}$, $\beta_{\perp}$ and b_{θ}. Before the neutral beam pulse, the plasma pressure is isotropic and may be determined from measured profiles of plasma density and electron and ion temperatures. During the neutral beam pulse, the total pressure profiles cannot be determined in this way because in this particular experiment the

fast ion distribution is strongly anisotropic (CLARK et al., 1980). However numerical solutions of (32) indicate that $\Delta(r)$ is relatively insensitive to the detailed shape of $\beta_{\parallel}(r)$, and $\beta_{\perp}(r)$ when compared with their average values. At the plasma edge these may be calculated from magnetic measurements as follows. At r = a (32) may be expressed as:

$$(\Lambda + 1) = \bar{\beta}_{\perp} + \bar{\beta}_{\parallel} + \frac{1}{2} L_i \qquad \ldots (53)$$

where Λ is the coefficient of asymmetry and L_i the internal inductance (MUKHOVATOV and SHAFRANOV, 1971). $\bar{\beta}_{\perp}$ may be measured directly using a plasma diamagnetic loop and L_i may be calculated from (29) by assuming $j(r)$ is proportional to $T(r)^{3/2}$. Λ may be determined from the value of the vertical magnetic field, B_v, required for plasma equilibrium, viz:

$$B_v = \frac{\mu_o I_p}{4\pi R_o} \left[\ell n(8R_o/a) + \Lambda - \frac{1}{2} \right] \qquad \ldots (54)$$

where I_p is the plasma current. Thus before neutral beam heating (32) and (34) were solved using measured profile data of density and temperatures, the profile value of β_p being consistent with the magnetic measurements. During the heating pulse, the measured profile data were used in conjunction with profiles of $\beta_{\parallel}$ and $\beta_{\perp}$ for the fast ions of the form (18) with p = 2 and q = 2. The peak values of these were chosen so as to provide edge values of $\bar{\beta}_{\parallel}$ and $\bar{\beta}_{\perp}$ which were consistent with the magnetic measurements of β_p and Λ.

The results for both Δ and Δ_{ece} are compared with the experimental

data in fig 15 where the magnetic axis has been equated to the current axis. Before the heating pulse the discrepancy between Δ and Δ_{ece} is $\sim$ 6mm in the centre because the plasma is paramagnetic ($\beta_p \sim 0.4$) whereas during the pulse the plasma diamagnetism is very small ($\beta_p \sim 1$) and the discrepancy correspondingly small (q.v. section 2.5). For this case the plasma magnetic field correction is shown in fig 14(b).

Overall agreement between calculation and measurement in fig 15 is good considering that an accuracy of better than $(r/R)^2$ is required of T(R). In particular: i) the absolute position of the temperature profile centre agrees with the plasma current position to within 0.2% of R_o which is less than the measurement errors associated with the flux loops or the toroidal field coil current; ii) the increased shift of the flux surface centres associated with the increased β_p on heating is clearly detected by the ECE profile; iii) agreement is reasonable over 60% of the minor radius. The large discrepancy which occurs for r > .15m is thought to be due to residual measurement errors on the edge of the second harmonic profile where the signal level is low, possibly because the instrument function is not ideal (q.v. section 3.4).

The assumption that the temperature surfaces can be identified with the flux surfaces is not surprising since electron thermal conduction along the magnetic field lines is very high. Also the displacement of the electron drift orbit surfaces from the flux surfaces is $\sim q_a r_L$ for free passing electrons and $\sim q_a r_L \sqrt{R_o}/a$ for trapped electrons, where r_L is the larmour radius (ARTSIMOVICH, 1972). In DITE these displacements are no greater than 4mm.

4.4 Analysis of the Third Harmonic Emission

The spectrum corresponding to the T(R) profile of fig 13(b) is shown in fig 16. Using the wall reflection model described in section 2.2, the density profile may be determined from (14) by Abel inversion of the I_o/R profile for the third harmonic and dividing by $T^3(r)$ derived from the second harmonic. Figure 17 shows the result of this for a value of $(1 - \rho)A$ which corresponds to $\rho = 0.984$ for a nominal value of $A = 22\,m^2$.

The upturn of $n_e(r)$ for $r > 60mm$ is incorrect suggesting that a complete solution of (5) and (7) is required for both harmonics. Thus for the second harmonic, using the $n_e(r)$ profile derived from the laser scattering and microwave diagnostics, the profiles of $\tau(R)$ and $\langle 1-e^{-\tau} \rangle$ may be calculated from (11) and (10) (see fig 18). Then expressing (5) in terms of the radiation (i.e. measured) temperature profile on axis, $T_r(R)$:

$$T_r(R) = T(R)\left[1 - e^{-\tau}\right] + \overline{T(R)}e^{-\tau} \qquad \ldots (55)$$

a solution for T(R) may be obtained by iteration using $T_r(R)$ as an initial estimate until a self-consistent result is obtained; (the iteration converges rapidly except at the edges of the profile). The percentage correction, $\delta T/T$ to be applied to the measured profile is shown in fig 14(a) illustrating that, given the high wall reflectivity, an average self-absorption of only 20% requires a correction of the same order. However because of the T^3 factor, this magnitude is trebled when the $n_e(r)$ profile is de-convolved from the third harmonic profile.

The corresponding $\tau(R)$ profile of the third harmonic is shown in fig 19 along with the correction to be made to $I_o(R)/R$ before Abel inversion, i.e. the relative magnitude of the second term compared with the first in the denominator of (7), which increases with τ until the emission becomes optically thick by means of reflections (8).

The final result for $n_e(r)$ is shown in fig 20(b) along with the initial assumption used to calculate the optical depth corrections. Here a self-consistent solution of (5) for the third harmonic is obtained by iteration of $n_e(r)$. Figure 20(a) shows the result of the same analysis at a lower density (i.e. the spectrum corresponding to fig 13(a)) which does not give as good agreement. Also shown are the laser scattering data for $n_e(r)$ taken over the series of discharges, the absolute values being calibrated by the 2mm interferometer data. Figure 21 shows the comparison between central densities, n_o deduced by this analysis from ECE spectra during one discharge and from the laser scattering data over 12 discharges. The value $\rho = 0.984$ was chosen so as to give the best agreement between the two methods of measuring n_o.

Provided optical depth corrections are included, the agreement between the two measurements of central density is to within 10% over a factor of 3 in density range. The main correction required at higher densities (fig 19) is due to the increase of self-absorption of the third harmonic compared with the wall absorption. The agreement between the profile measurements appears to break down beyond 1/3 of the minor radius. This is thought to be due to inaccuracies in the measurement of $I(\omega)$ at low levels and moreover, the problem of harmonic overlap (BARTLETT and COSTLEY, 1979) prevents the measurement of the third harmonic intensity over the whole cross-section of the plasma. However the results for n_o shown in fig 21 support the wall reflection

model as the amplitude of the third harmonic varies by a factor of 4 over the range of data shown. Measurement of the density by this method does require at least one calibration point in order to determine the wall reflection coefficient ρ.

5. CONCLUSION

With the exception of the frequency response calibration, the systematic corrections to the elementary $I(\omega)$ to $T(R)$ transformation are small in DITE. This is largely a consequence of the fact that, for the large aspect ratio ($R_o/a = 4.5$) it is possible to infer the spatial temperature distribution from the ECE spectrum viewed in the meridian plane. For large volume, non-circular cross-section plasmas this is no longer the case and in particular (i) well collimated optics are required for viewing ECE off the meridian plane, (ii) the radiation temperature of ECE from regions off the meridian plane where $\tau < 1$ will not equal the local electron temperature and (iii) corrections to the vacuum magnetic field require a full solution of the plasma MHD equilibrium. However the larger optical depths expected in these plasmas will help offset these disadvantages. Higher temperatures will also cause the resonance layer width correction to increase.

The configuration of the electron temperature surfaces in DITE inferred from the corrected temperature profile in the meridian plane is consistent with the calculated MHD equilibrium over most of the plasma cross-section. This suggests the possibility of using this analysis to derive $\beta(r)$ or $B_\theta(r)$ directly from ECE spectral measurements.

The isotropic wall reflection model requires a reasonable value for the wall reflectivity to explain the peak third harmonic intensity,

given the central electron temperature and density. However the density profile derived from the profile of the third harmonic does not appear to be reliable beyond r/a = 1/4. Although this might be improved by more accurate measurements of the emission at the base of the third harmonic, the diagnostic potential of this analysis is somewhat limited, particularly in small aspect ratio tokamaks where the harmonic overlap prevents the higher harmonics from being well defined in the ECE spectrum.

ACKNOWLEDGEMENTS

The author gratefully acknowledges the following: Dr. A.N. Dellis for construction and design of the waveguide antenna, Dr. P.J. Fielding for use of his ray-tracing code, Mr. A. Currie for computational assistance, the DITE physics team for providing diagnostic data and analysis, Dr. J. Hugill for critical discussions of the MHD equilibrium analysis and wall reflection model and Dr. J.W.M. Paul for his interest and encouragement.

REFERENCES

ADVANCED KINETICS LTD., 1231 Victoria St., Costa Mesa Ca., 92627, USA.

ARTSIMOVICH, L.A., (1972) Nucl. Fusion 12, 215.

BAGDASAROV, A.A., CLARK, W.H.M., COSTLEY, A.E., GORBUNOV, E.P., and NEILL, G.F. (1979) Proc. 9th European Conf. Controlled Fusion and Plasma Physics, Oxford Vol I, paper EP12.

BARTLETT, D.V. and COSTLEY, A.E. (1979) National Physical Laboratory Report DES 53, London.

BEKEFI, G. (1966a) "Radiation Processes in Plasmas", Wiley, New York, p 40.

BEKEFI, G. (1966b) Ibid. p 314.

BORNATICI, M. (1980) Proc. Autumn College on Plasma Physics Trieste, 520-H4-4.

BORNATICI, M., ENGELMANN, F., NOVAK, S. and PETRILLO, V. (1981) Plasma Physics 23, (12) 1127.

BOYD, D.A. (1980) Proc. Joint Workshop on ECE and ECRH, Oxford, Culham Laboratory Report, CLM-ECR(1980), p. 113.

BRACEWELL, R. (1965) "The Fourier Transform and its Applications", McGraw-Hill, New York, p. 262.

BROSSIER, P., COSTLEY, A.E., KOMM, D.S., RAMPONI, G. and TAMOR, S. (1977) Proc. 6th Int. Conf. Plasma Physics and Controlled Nuclear Fusion Research, Berchtesgaden, West Germany, IAEA, Vienna, 2, 409.

CHANTRY, G.W. and FLEMMING, J.W. (1976) Infrared Physics 16, 655.

CLARK, W.H.M. (1980) Proc. Joint Workshop on ECE and ECRH, Oxford Ibid. p. 221.

CLARK, W.H.M., CORDEY, J.G., COX, M., GILL, R.D., HUGILL, J., PAUL, J.W.M. and START, D.F.H. (1980) Phys. Rev. Lett. 45 (13), 1101.

COSTLEY, A.E., BAKER, E.A.M., BARTLETT, D.V., CLARK, W.H.M., KIFF, M.G., and NEILL, G.F. (1980) National Physical Laboratory Report, DES 62, London, Appendix D.

COSTLEY, A.E. and CHAMBERLAIN, J. (1974) Proc. Precision of Electromagnetic Measurements, IEE, No. 113, 210-212.

COSTLEY, A.E., HASTIE, R.J., PAUL, J.W.M. and CHAMBERLAIN, J. (1974) Phys. Rev. Lett. 33, 758.

COSTLEY, A.E. and T.F.R. GROUP, (1977) Phys. Rev. Lett. 38, (25) 1477.

CONNOR, J.W. and HASTIE, R.J. (1976) Physics of Fluids, 19, (11) 1727.

EFTHIMION, P.C. (1979) Rev. Sci. Instrum. 50, 949.

ENGELMANN, F. and CURATOLO, M. (1973) Nucl. Fusion 13, 497.

HOSEA, J., ARUNSALAM, V. and CANO, R. (1977) Phys. Rev. Lett. 39, 888.

HUTCHINSON, I.H. and KISSEL, S.E. (1979) 4th Int. Conf. Infrared and Millimetre Waves, Miami.

HUTCHINSON, I.H. and KOMM, D.S. (1977) Nucl. Fusion 17, 1077.

LEWIS, E.V. (1963) "Statistical Analysis", Van Nostrand, New York, p. 162.

MARTIN, D.H. and LESURF, J. (1978) Infrared Physics 18, 405.

MARTIN, D.H. and PUPLETT, E. (1970) Infrared Physics 10, 105.

MARTIN, T.J. (1976) COMPUMAG Conf. Oxford, Culham Laboratory pre-print CLM-P460.

MORENO, T. (1948) "Microwave Transmission Design Data", Dover, New York, p.222.

MUKHOVATOV, V.S. and SHAFRANOV, V.D. (1971) Nucl. Fusion 11, 605.

NAVE, M.F. and CLARK, W.H.M. (1980) Proc. Joint Workshop on ECE and ECRH, Oxford, Ibid. p 81.

PAUL, J.W.M. et al. (1976) Proc. 6th Int. Conf. Plasma Physics and Controlled Nuclear Fusion Research, Berchtesgaden, West Germany, IAEA, Vienna, 2, 269.

PRENTICE, R. (1978) Culham Laboratory Report CLM-R179, HMSO, London.

QMC INSTRUMENTS LTD. 229 Mile End Road, London E1 4AA.

ROSENBLUTH, M.N. (1970) Nucl. Fusion 10, 340.

SAKAI, K., KAWAHATA, K., SATO, M., NODA, N., IWAMA, N., INOUE, A. and TSUKISHMA, T. (1980) Proc. 5th Int. Conf. Infrared and Millimetre Waves U. Wurzburg, West Germany, p 341.

SHAFRANOV, V.D. (1962) Atomn. Energ. 13, 521.

STIX, T.H. (1962) "The Theory of Plasma Waves", McGraw-Hill, New York.

TAMOR, S. (1981) Science Applications Inc., Report LAPS-72.

TAIT, G.D., STAUFFER, F.J. and BOYD, D.A. (1982) Phys. Fluids 24 (4), 719.

APPENDIX

Asymptotic approximations for $F(\tau_o)$

a) $\tau_o << 1$

In this limit, the $e^{-\tau}$ factor in the integrand (26) is approximately unity over the range of integration, thus:

$$F(\tau_o) \simeq \tau_o \int_o^1 y(\xi)\, d\xi = \tau_o \int_o^\infty (1 - \xi)\, dy \qquad \ldots (A1)$$

where $$\frac{\tau}{\tau_o} = \xi(y) = \mathrm{erf}(\sqrt{y}) - \frac{\sqrt{y}\, e^{-y}}{15\sqrt{\pi}} (8y^2 + 20y + 30) \ldots (A2)$$

After substitution of (A2) into (A1) the integration can be carried out by making use of the properties of repeated integrals of the error function (ABRAMOWITZ and STEGUN, 1965). This leads to:

$$F(\tau_o) \simeq \frac{7}{2} \tau_o \qquad \ldots (A3)$$

b) $\tau_o >> 1$

In this limit, the $e^{-\tau}$ factor in the integrand (26) decays rapidly over the range of integration such that the inversion $\tau(y)$ can be evaluated for small y. Thus expanding the integrand of (22) to second order leads to:

$$t = y^{7/2}\left(1 - \frac{7}{9}y + \frac{7}{22}y^2\right)$$

where:
$$t = \tau \frac{105\sqrt{\pi}}{16\tau_o} = \tau \frac{A}{\tau_o}$$

By expressing y as a power series in $t^{2/7}$ and evaluating it to second order:

$$y = t^{2/7}\left(1 + \frac{2}{9}t^{2/7} + \frac{62}{891}t^{4/7}\right)$$

(26) can be integrated to give:

$$F(\tau_o) = \left(\frac{A}{\tau_o}\right)^{2/7}\left\{\Gamma(9/7) + \frac{2}{9}\left(\frac{A}{\tau_o}\right)^{2/7}\Gamma(11/7) + \frac{62}{891}\left(\frac{A}{\tau_o}\right)^{4/7}\Gamma(13/7)\right\}$$

Evaluating the constants gives:

$$F(\tau_o) = \frac{1.814}{\tau_o^{2/7}} + \frac{0.804}{\tau_o^{4/7}} + \frac{0.570}{\tau_o^{6/7}} \qquad \ldots (A4)$$

Numerical integration of (26) (see fig 4(b)) indicates that approximation (A3) is accurate to better than 10% for $\tau_o < 0.1$ and approximation (A4) accurate to better than 10% for $\tau_o > 3$.

REFERENCES

ABRAMOWITZ, M. and STEGUN, I.A. (ed) (1965), "Handbook of Mathematical Functions", p299, Dover, New York.

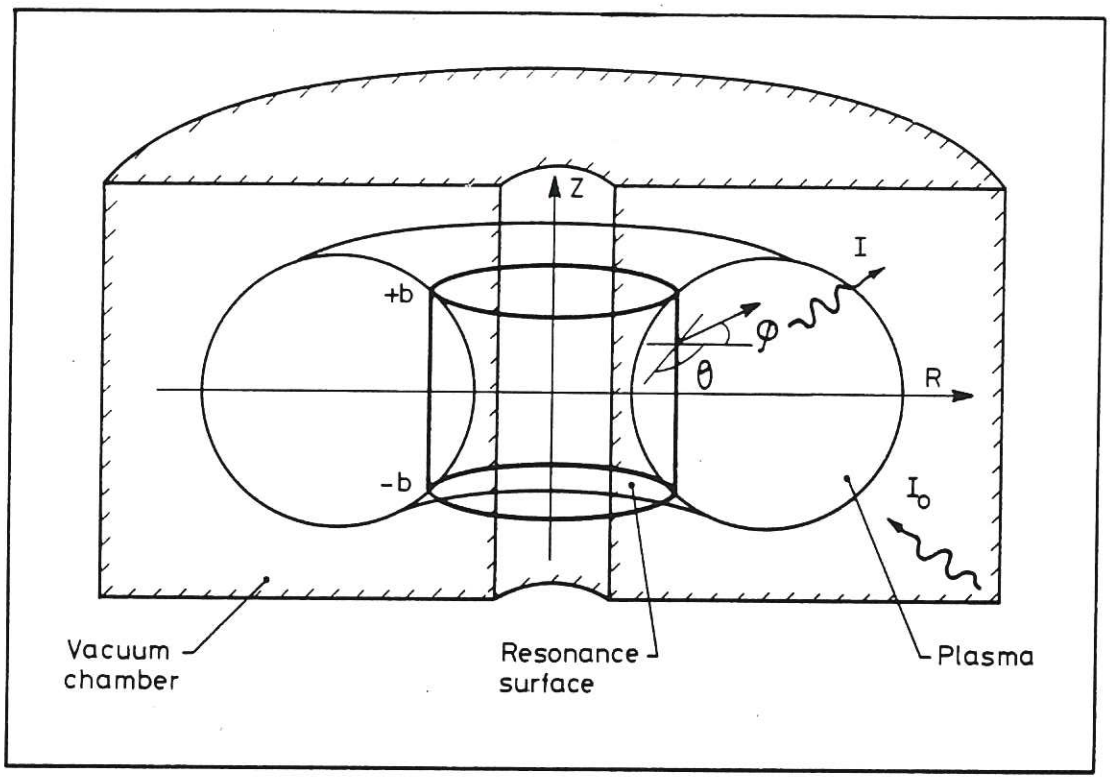

Fig.1 Isotropic wall reflection model.

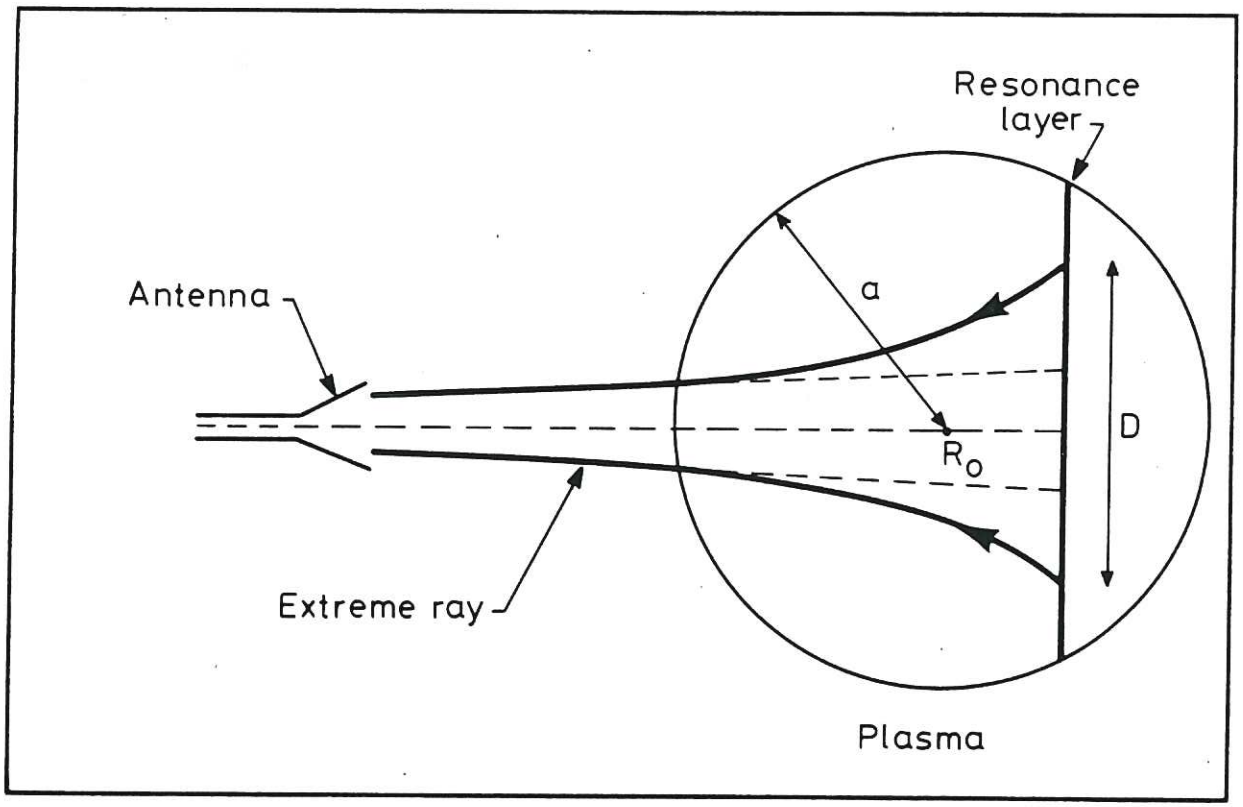

Fig.2 Effect of refraction on antenna pattern.

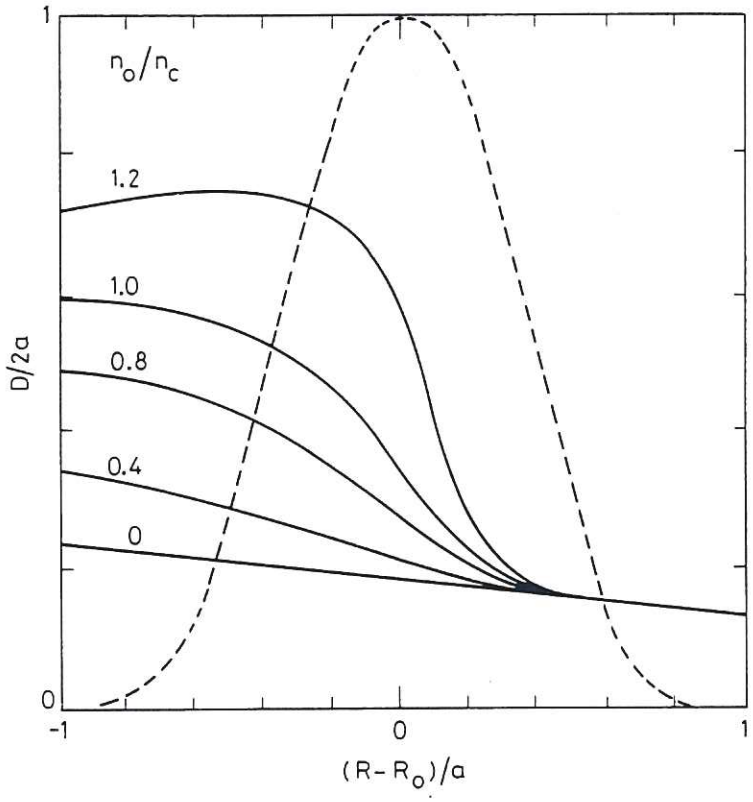

(a) Peaked profile (p = 2, q = 4)

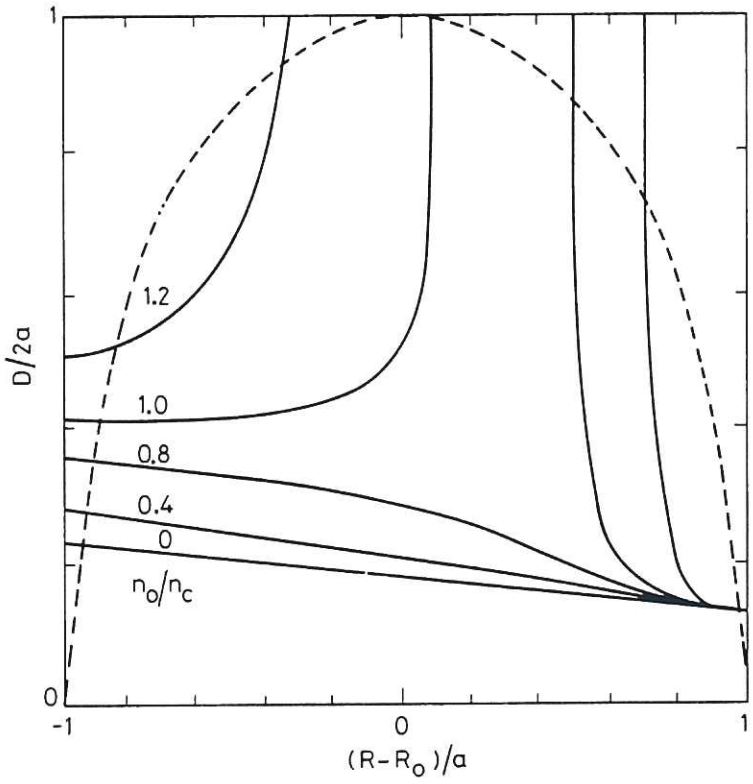

(b) Flat profile (p = 2, q = 0.5)

Fig.3 Radial variation of antenna dimension D for different central densities n_o (solid line) and form of density profile (dashed line).

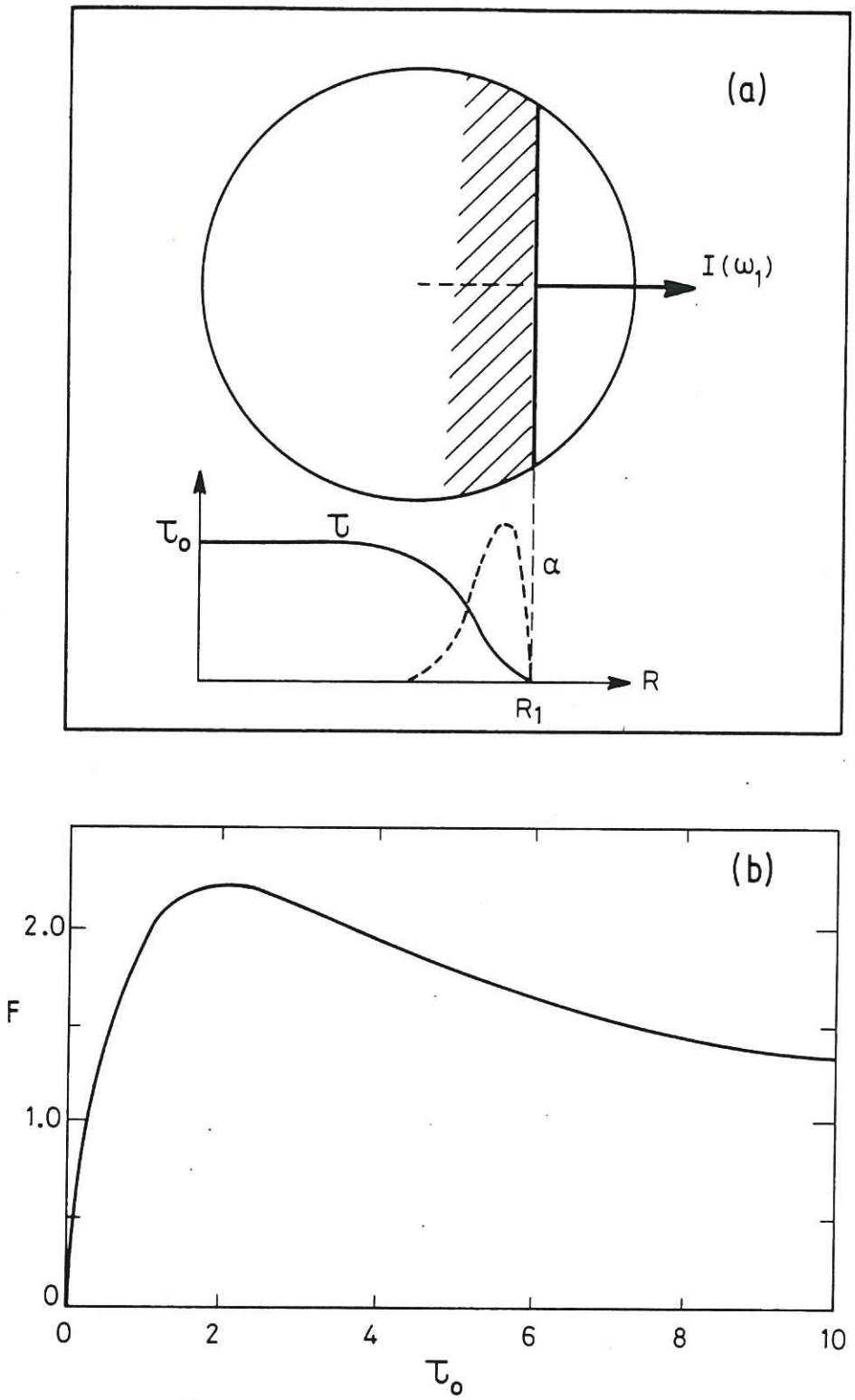

Fig.4(a) Variation of absorption coefficient α and optical depth τ through resonance layer R_1.
(b) Relativistic resonance layer width function $F(\tau_o)$.

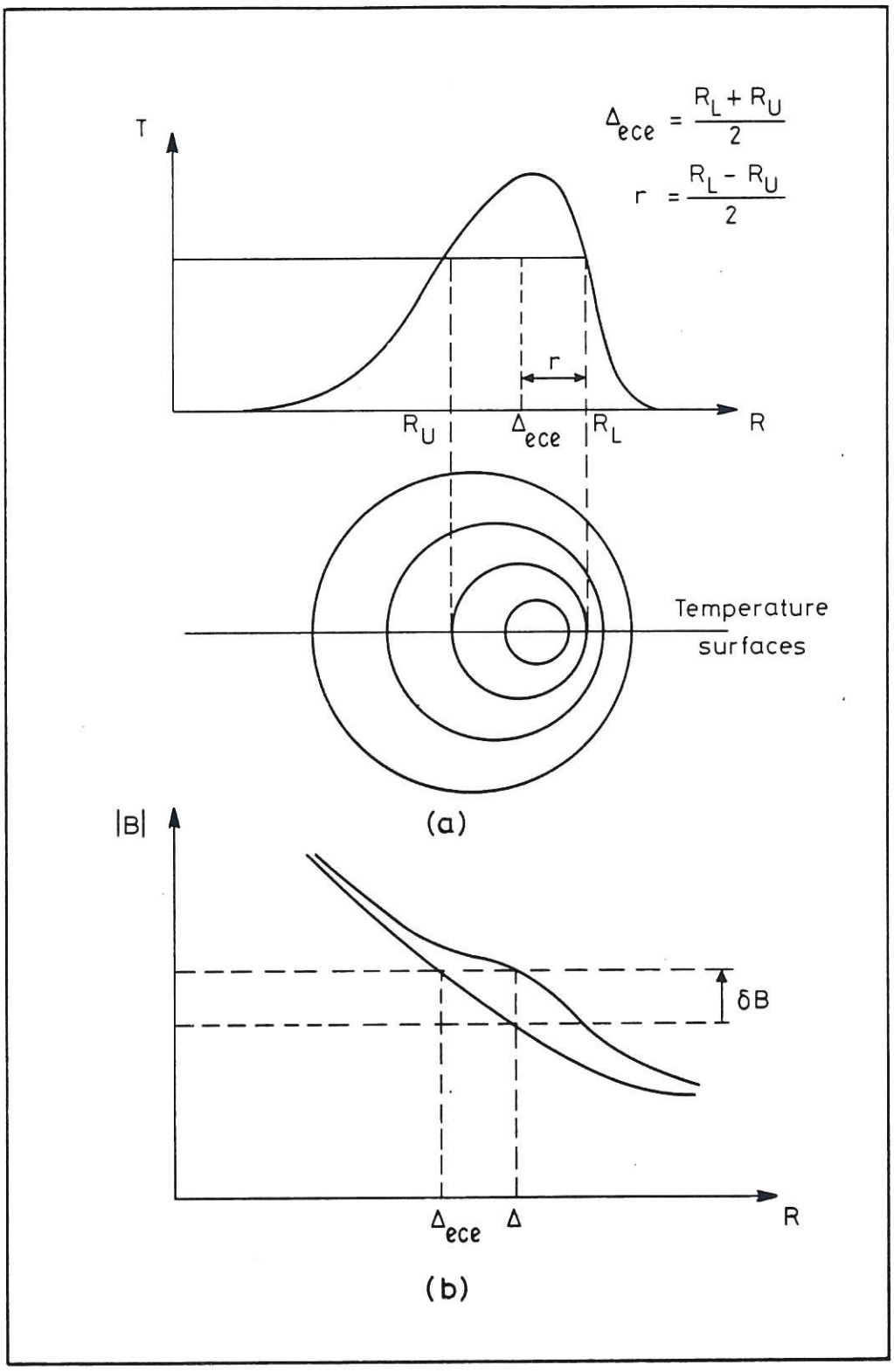

Fig.5(a) Relation between circular cross-section temperature surfaces and temperature profile T(R).
(b) Effect of magnetic field correction δB on observed temperature surface shift Δ_{ece} assuming a vacuum magnetic field.

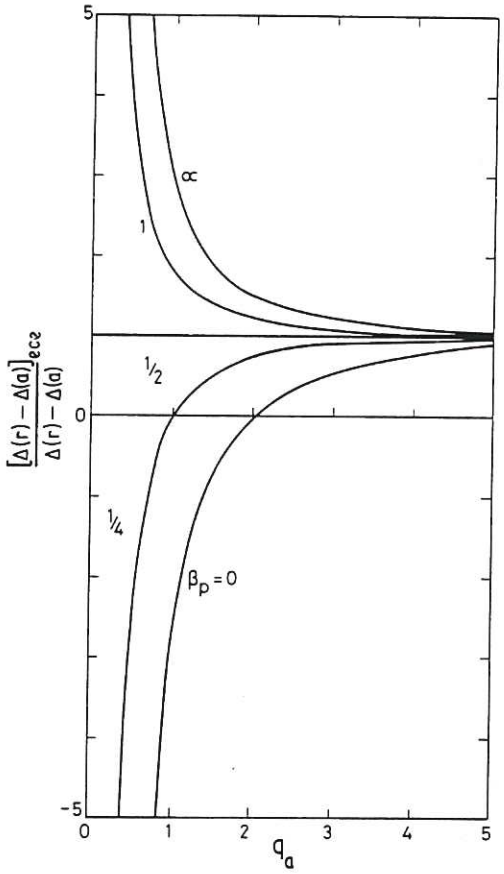

Fig.6 Variation of ECE to Shafranov shift ratio with poloidal beta, β_p, and safety factor q_a for a parabolic pressure profile and a uniform current density.

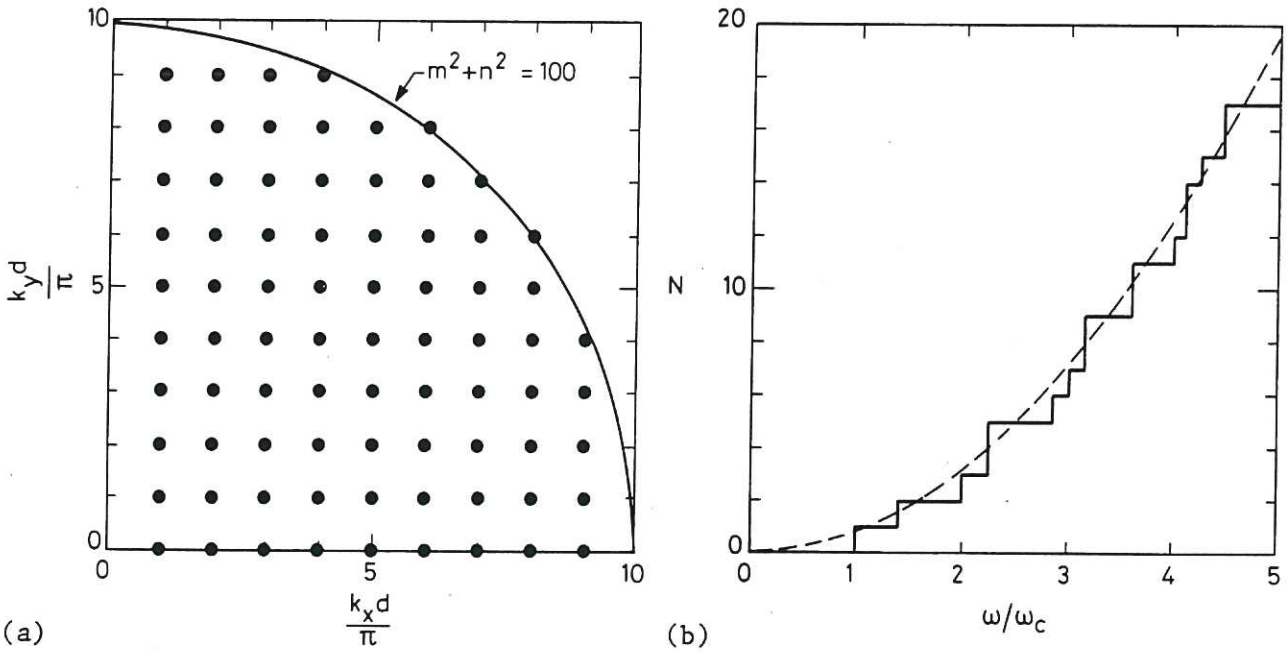

Fig.7(a) Perpendicular wave-number space for a square cross-section waveguide showing the number of propagating TE modes for $\omega = 10\omega_C$.

(b) Number of modes N propagating in a square waveguide as a function of frequency (solid line) and the blackbody continuum $\pi/4(\omega/\omega_C)^2$ (dashed line).

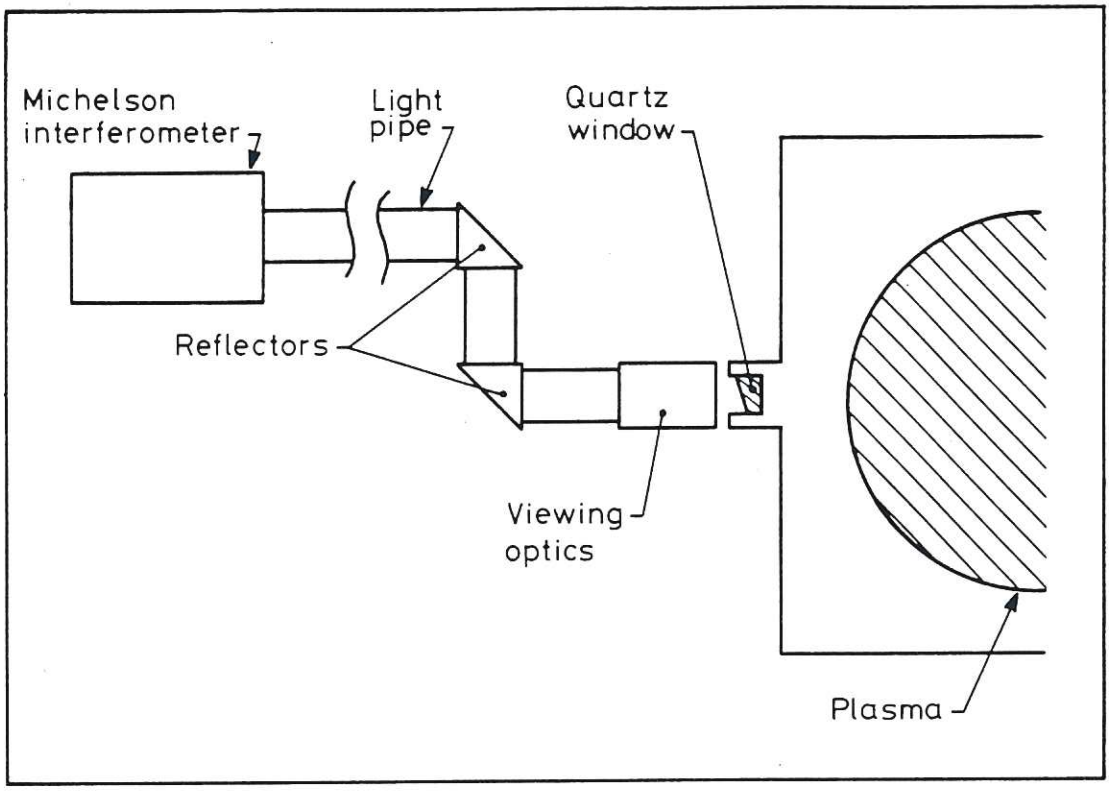

Fig.8 Schematic arrangement of Michelson interferometer to measure ECE.

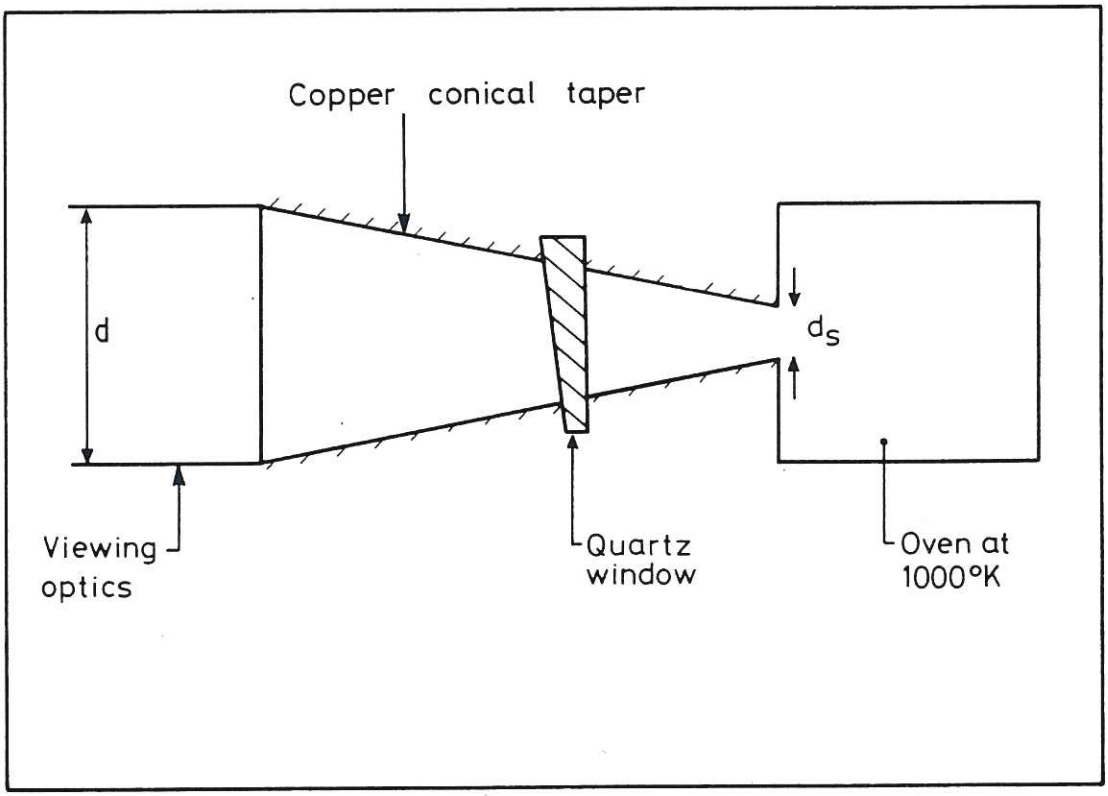

Fig.9 Blackbody calibration source for Michelson interferometer.

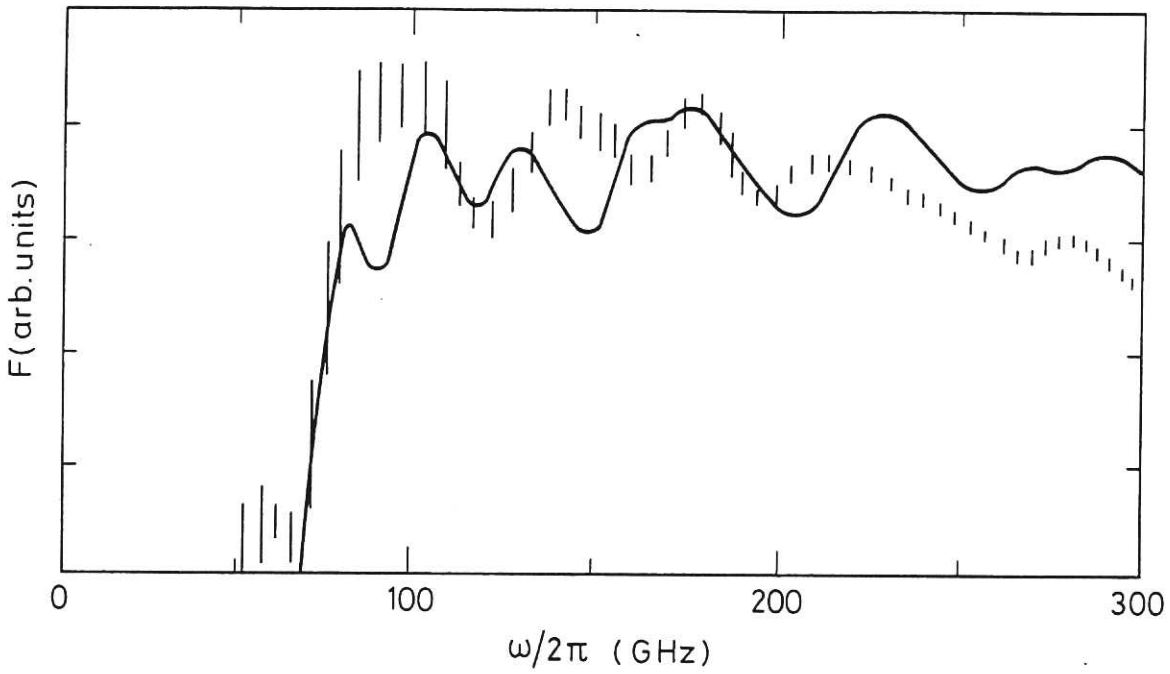

Fig.10 Comparison between the measured frequency response F of the instrument and lens optics (bars) and the theoretical frequency response of a cylindrical waveguide (solid line) for fundamental cut-off frequency $\omega_C/2\pi = 75$ GHz and interferometer path difference $\ell = 26$ mm.

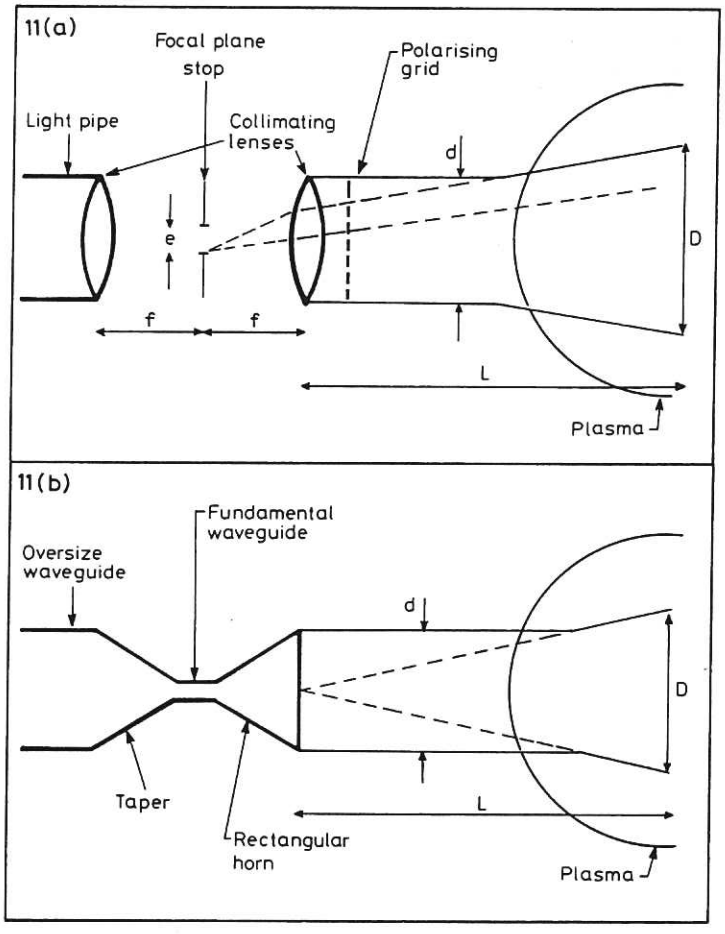

Fig.11(a) Lens collimation optics.
(b) Waveguide horn antenna.

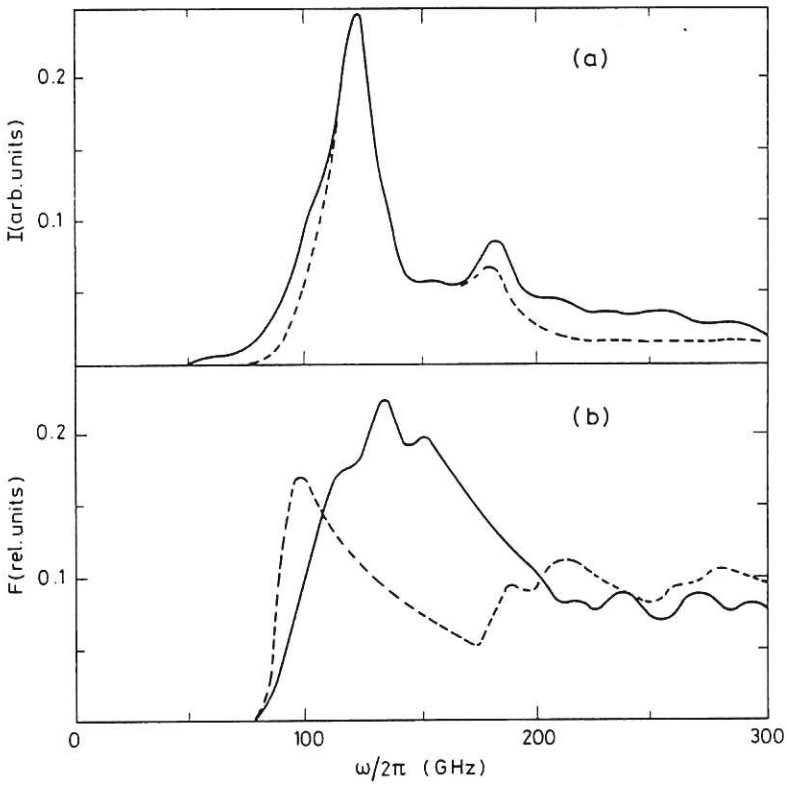

Fig.12(a) Calibrated non-thermal ECE spectrum measured with the lens optics (solid line) and the corresponding uncalibrated spectrum measured with the waveguide antenna (dashed line). Both spectra scaled to be equal at 120 GHz.

(b) Frequency response F of the waveguide antenna (solid line) derived from the absolute ratio of the spectra in (a) and the theoretical frequency response of a rectangular waveguide (dashed line), cut-off frequency 90.9 GHz.

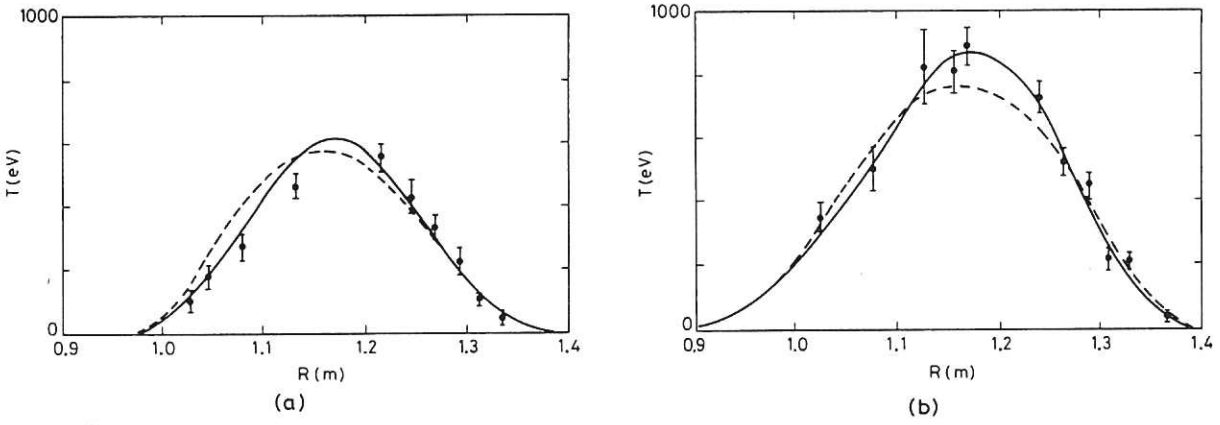

(a) before neutral beam heating and (b) during neutral beam heating.

Fig.13 Least squares comparison of calibrated (solid line, $\chi^2 = 1.2$) and uncalibrated (dashed line, $\chi^2 = 2.4$) ECE temperature profiles with laser scattering measurements:

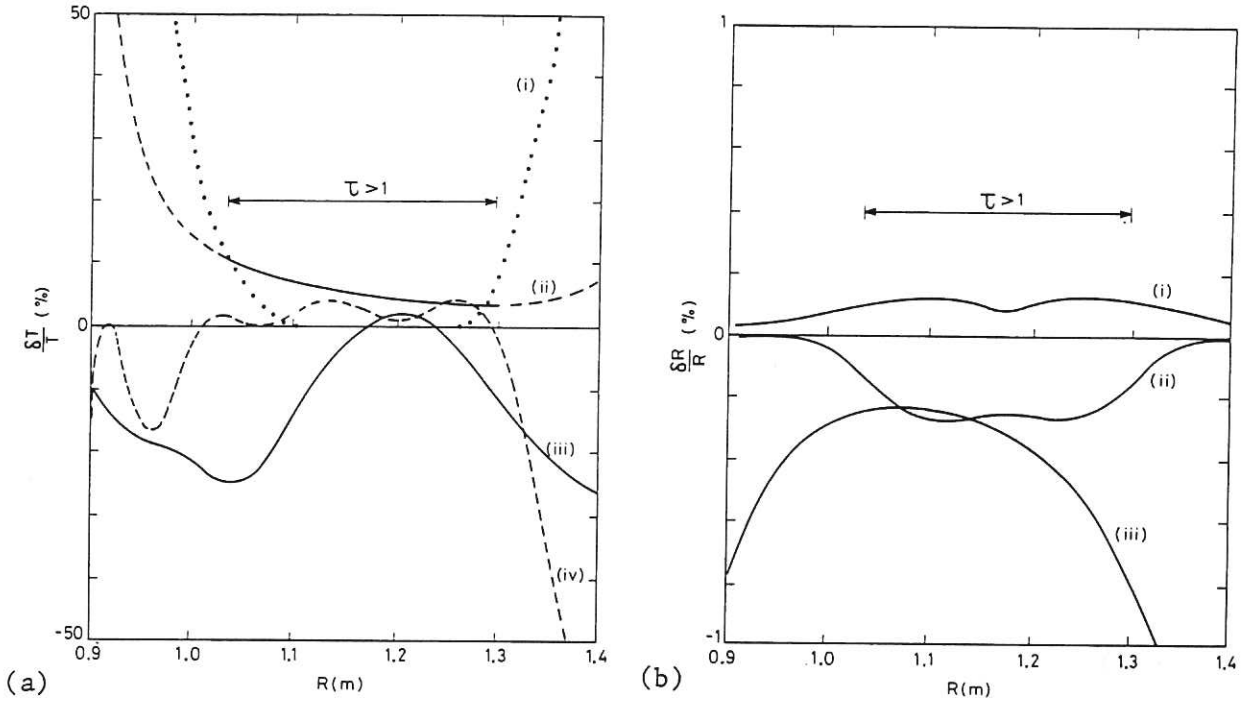

Fig.14(a) Percentage systematic corrections $\delta T/T$:
- (i) finite optical depth correction,
- (ii) refraction of antenna pattern correction,
- (iii) instrumental frequency response correction (normalised to unity at $R_o = 1.17$),
- (iv) instrumental resolution error correction.

(b) Percentage systematic corrections $\delta R/R$:
- (i) magnetic field correction ($\beta p \sim 1$),
- (ii) resonance layer width correction,
- (iii) vacuum field ripple correction.

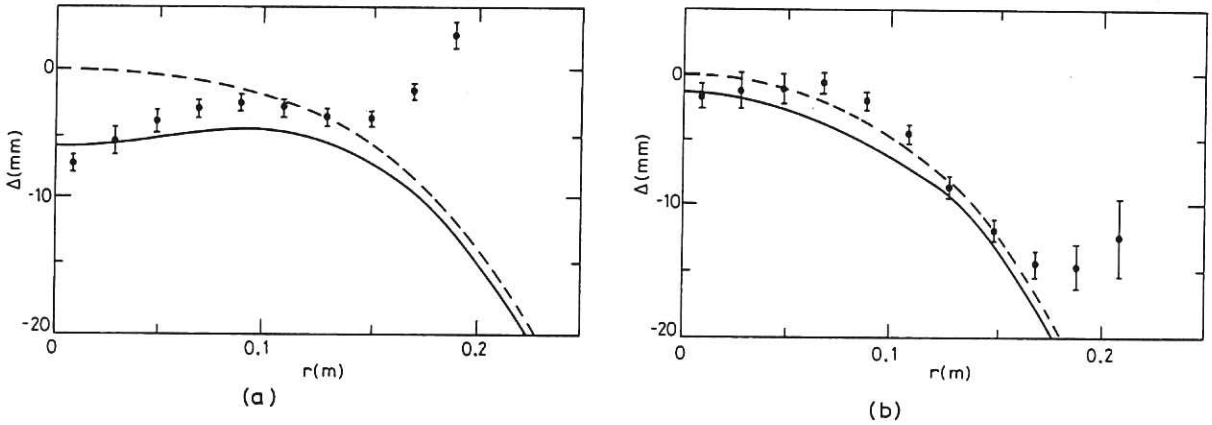

Fig.15 Comparison between the measured ECE shift (points), the expected ECE shift (solid line) and the true Shafranov shift (dashed line);
(a) before neutral beam heating,
$L_i = 2.06, \beta_p = 0.42, \Lambda = 0.46, q_a = 6.5$
(b) during neutral beam heating
$L_i = 1.82, \beta_p = 1.02, \Lambda = 1.95, q_a = 6.5$.

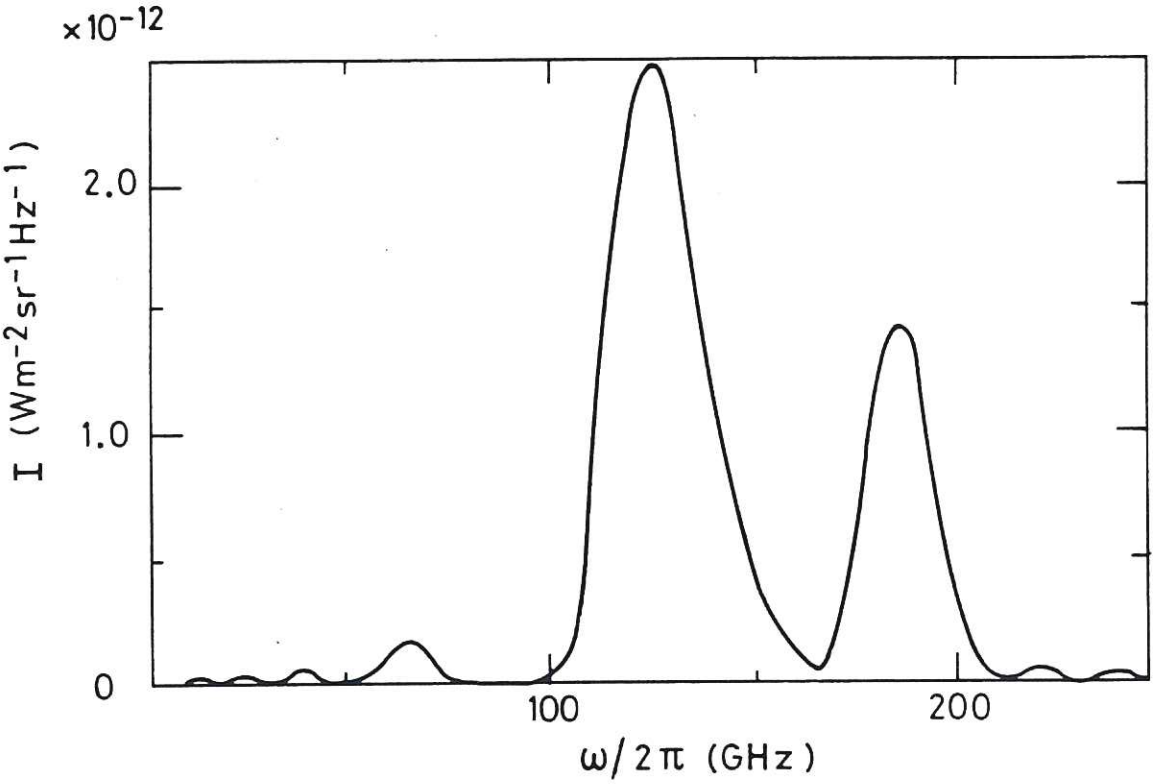

Fig.16 ECE spectrum for E mode during neutral beam heating.

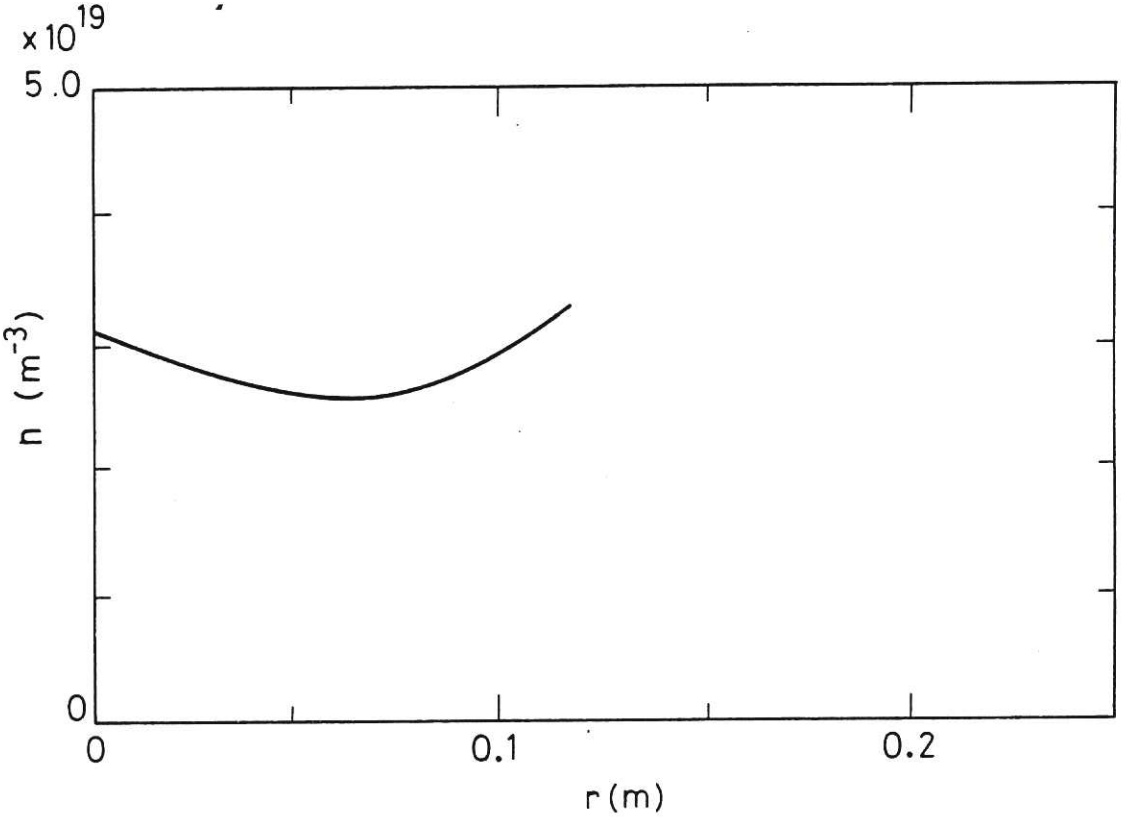

Fig.17 Uncorrected density profile n(r) derived from the third harmonic E mode emission for wall reflectivity $\rho = 0.984$ and wall area $A = 22\,m^2$.

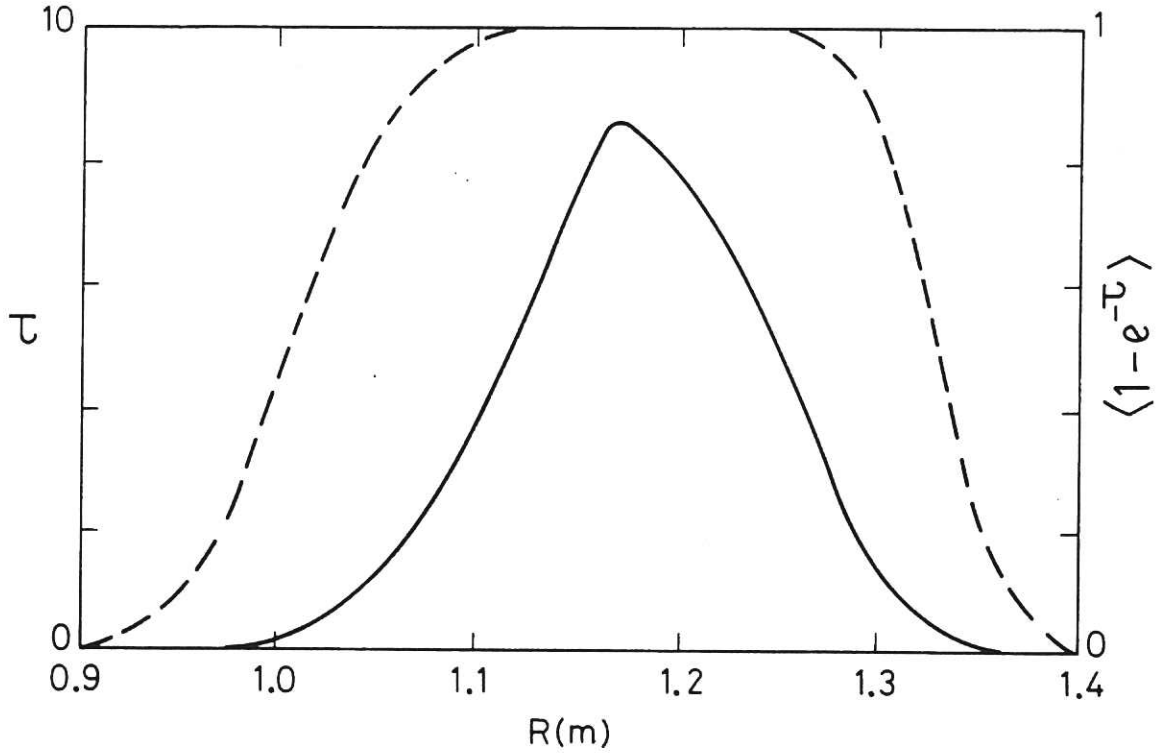

Fig.18 Radial variation of the optical depth τ (solid line) and the solid angle average value of the self-absorption $\langle 1-e^{-\tau} \rangle$ for the second harmonic E mode.

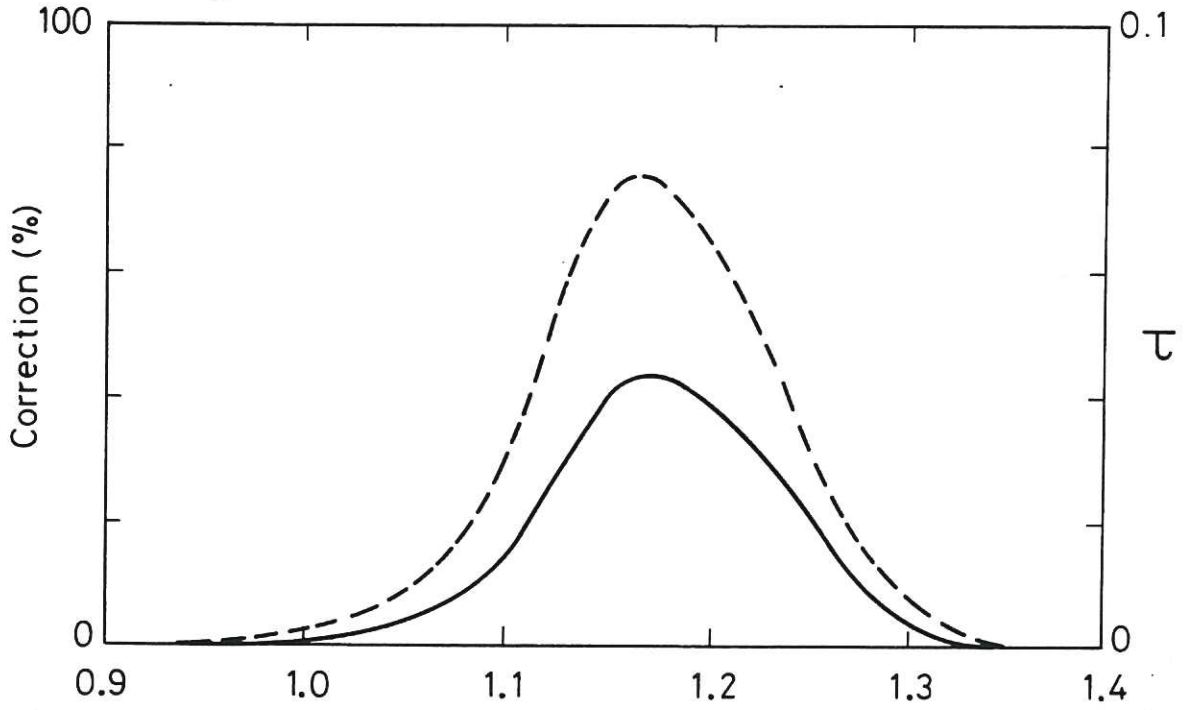

Fig.19 Radial variation of the optical depth τ (dashed line) for the third harmonic E mode and the percentage correction (solid line) to the profile of I_o/R before inversion to the density profile.

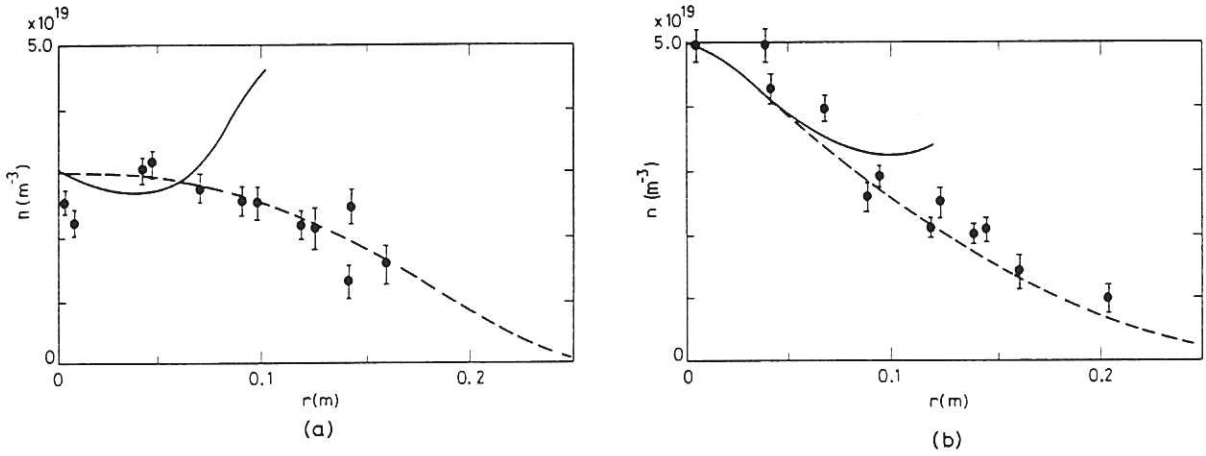

(a) before neutral beam heating

(b) during neutral beam heating.

Fig.20 Comparison between density profiles n(r) from ECE (corrected) and laser scattering for wall reflectivity $\rho = 0.984$; (dashed lines represent the functional form (18) assumed for n(r)):

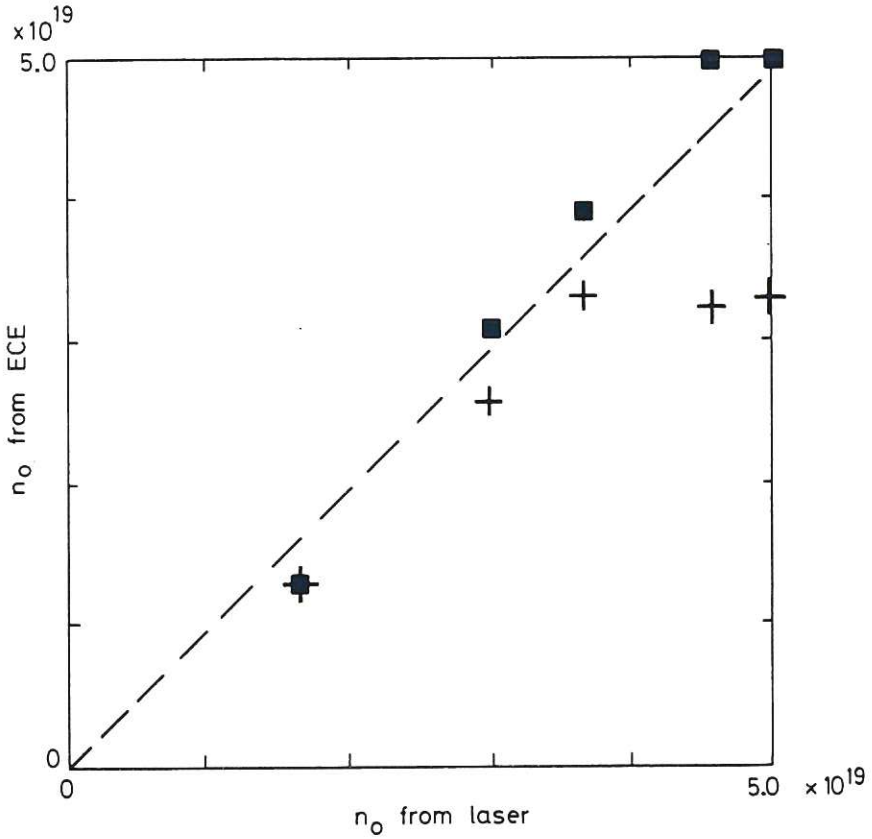

Fig.21 Comparison of measurements of central density n_0 from ECE and laser scattering for wall reflectivity $\rho = 0.984$; (squares are corrected ECE data, crosses uncorrected data).